

## A bosonic Josephson junction

This content has been downloaded from IOPscience. Please scroll down to see the full text.

2007 J. Phys. B: At. Mol. Opt. Phys. 40 R61

(<http://iopscience.iop.org/0953-4075/40/10/R01>)

View [the table of contents for this issue](#), or go to the [journal homepage](#) for more

Download details:

IP Address: 147.142.186.54

This content was downloaded on 18/09/2015 at 10:26

Please note that [terms and conditions apply](#).

## TOPICAL REVIEW

# A bosonic Josephson junction

**R Gati and M K Oberthaler**Kirchhoff-Institut für Physik, Universität Heidelberg, Im Neuenheimer Feld 227,  
69120 Heidelberg, GermanyE-mail: [bec@matterwave.de](mailto:bec@matterwave.de)

Received 7 November 2005, in final form 21 March 2007

Published 1 May 2007

Online at [stacks.iop.org/JPhysB/40/R61](http://stacks.iop.org/JPhysB/40/R61)**Abstract**

We review the experimental realization of a single bosonic Josephson junction for ultracold gases, which was made possible by the generation of a precisely controllable double-well potential for Bose–Einstein condensates. We will focus on the comparison of the experimentally obtained data with the predictions of a many-body two-mode model and a mean-field description and show that the observed static, thermal and dynamical properties can be described in terms of classical equations.

**1. Introduction**

The difference between classical and quantum mechanical dynamics becomes strikingly evident when two macroscopic quantum objects are weakly coupled to each other. This fact was understood by the Nobel laureate Brian D Josephson in 1962 [1], when he predicted the counter-intuitive effect that a direct current can flow between two superconductors coupled via an insulating thin layer although no external voltage is applied, which is called the dc-Josephson effect. Furthermore, an external voltage will in this system not result in a direct current but gives rise to a rapidly oscillating current; this effect is known as the ac-Josephson effect. Very soon, after the first experimental proof of principle [2], the Josephson effects found their way to various applications such as voltage standards (Shapiro effect) and ultrasensitive magnetic field sensors (SQUIDS). Also fundamental questions on quantum physics were and are extensively studied theoretically as well as experimentally with Josephson junctions in different configurations [3, 4], ranging from ultra small junctions to long junction arrays.

Since the Josephson junction dynamics ‘only’ relies on the existence of two weakly coupled macroscopic quantum states, similar behaviour has been observed in experiments with two superfluid helium baths coupled through nano-apertures. The first superfluid Josephson junctions were generated with superfluid  $^3\text{He}$  in 1997 [5–7] and with  $^4\text{He}$  2001 [8]. With the advent of Bose–Einstein condensates of weakly interacting gases [9–11] a new experimental system has become available for the quantitative investigation of Josephson effects in a very well controllable environment, as was discussed already in 1986 [12].

In this review we will focus on the discussion of bosonic Josephson junctions (BJJ), generated by confining a single Bose–Einstein condensate (BEC) in a double-well potential. The Josephson junction in this system consists of the two localized matter wave packets in the two wells, which are weakly coupled via tunnelling of particles through the potential barrier. In the first part we will deal with the basic theoretical description of the physical situation. We discuss a reduced many-particle theory and connect the results to the mean-field description. In the following part we deal with the static, thermal and dynamical properties and compare the predictions of the many-particle theory and the mean-field theory to our experimental findings.

## 2. Theoretical description

In the experiment the Bose–Einstein condensate is confined in a double-well potential of the form

$$V_{\text{dw}} = \frac{1}{2}m(\omega_x^2 x^2 + \omega_y^2 y^2 + \omega_z^2 z^2) + \frac{V_0}{2} \left( 1 + \cos \frac{2\pi}{d_{\text{sw}}} x \right), \quad (1)$$

which consists of a 3D harmonic confinement and a 1D periodic potential acting as the barrier. The periodic potential has a height of  $V_0$  and a periodicity of  $d_{\text{sw}}$  and the harmonic trap is characterized by the three trapping frequencies  $\omega_x$ ,  $\omega_y$  and  $\omega_z$ .

Generally, this is a many-particle problem and the corresponding many-body Schrödinger equation cannot be solved exactly due to the interparticle interaction. However, in order to describe our experimental situation the dimension of the Hilbert space can be reduced drastically due to the special structure of the energy spectrum. The weak link, which generates the Josephson junction, directly results in a small energy splitting between the mean-field ground state and the first excited state of the double-well potential (see section 2.5). Thus, for low energetic excitations and low temperature only these two states will play a role and the influence of the higher lying states can be neglected. With this, the dimension of the Hilbert space is reduced to  $N + 1$ , where  $N$  is the number of particles in the Bose–Einstein condensate. The main difficulty when applying this two-mode approximation is to find the right wavefunctions or orbitals, which account for the two quasi-degenerate states. However, in the following we will assume that these states are known and present later a way how to calculate the corresponding wavefunctions.

### 2.1. Two-mode approximation—the Bose–Hubbard model

The two-mode approximation and the resulting two-mode model can be applied for investigating the steady state properties of the BJJ and for low energetic excitations. If the system cannot be described accurately by the two-mode model then multi-orbital theories like those discussed in [13, 14] have to be used. Following the derivation given in [15] or [16] the relevant many-particle energy functional is given by

$$\hat{H} = \hat{H}_0 + \hat{H}_{\text{int}}, \quad (2)$$

$$\hat{H}_0 = \int \mathbf{d}\mathbf{r} \left( -\frac{\hbar^2}{2m} \hat{\Psi}^\dagger \nabla^2 \hat{\Psi} + \hat{\Psi}^\dagger V_{\text{dw}} \hat{\Psi} \right), \quad (3)$$

$$\hat{H}_{\text{int}} = \frac{g}{2} \int \mathbf{d}\mathbf{r} \hat{\Psi}^\dagger \hat{\Psi}^\dagger \hat{\Psi} \hat{\Psi}, \quad (4)$$

where  $V_{\text{dw}}$  is the 3D double-well potential (equation (1)),  $g = \frac{4\pi\hbar^2 a}{m}$  is the coupling constant and  $a$  is the  $s$ -wave scattering length of the particles. Taking only the mean-field ground state

$\Phi_g$  and the mean-field first excited state  $\Phi_e$  into account, we can rewrite the wavefunction  $\hat{\Psi}$  as

$$\hat{\Psi} = \hat{c}_g \Phi_g + \hat{c}_e \Phi_e \quad \text{with} \quad \int d\mathbf{r} |\Phi_{g,e}|^2 = 1, \quad (5)$$

and with  $\hat{c}_g^\dagger$  and  $\hat{c}_e^\dagger$  ( $\hat{c}_g$  and  $\hat{c}_e$ ) being the creation (annihilation) operator for a particle in the ground and the excited state. The operators obey the standard bosonic commutation relation  $[\hat{c}_i, \hat{c}_j^\dagger] = \delta_{ij}$ . A more direct and convenient choice for the basis are the atom number states for which the expectation value of the population of the left and right well is sharp. The corresponding creation operators are  $\hat{c}_l = \frac{1}{\sqrt{2}}(\hat{c}_g + \hat{c}_e)$  and  $\hat{c}_r = \frac{1}{\sqrt{2}}(\hat{c}_g - \hat{c}_e)$ . In this basis  $\hat{\Psi}$  is given by

$$\hat{\Psi} = \frac{1}{\sqrt{2}}(\hat{c}_l(\Phi_g + \Phi_e) + \hat{c}_r(\Phi_g - \Phi_e)). \quad (6)$$

By inserting equation (6) into equation (3) we find

$$\begin{aligned} \hat{H}_0 &= \frac{1}{2}((\hat{c}_l^\dagger \hat{c}_l + \hat{c}_r^\dagger \hat{c}_r)(E_g + E_e) + (\hat{c}_l^\dagger \hat{c}_r + \hat{c}_r^\dagger \hat{c}_l)(E_g - E_e)) \\ &= N \frac{E_g + E_e}{2} + (\hat{c}_l^\dagger \hat{c}_r + \hat{c}_r^\dagger \hat{c}_l) \frac{E_g - E_e}{2}, \end{aligned} \quad (7)$$

with

$$E_{g,e} = \int d\mathbf{r} \left( -\frac{\hbar^2}{2m} \Phi_{g,e} \nabla^2 \Phi_{g,e} + \Phi_{g,e} V_{\text{dw}} \Phi_{g,e} \right), \quad (8)$$

and substituting into equation (4)

$$\begin{aligned} \hat{H}_{\text{int}} &= \hat{c}_l^\dagger \hat{c}_l^\dagger \hat{c}_l \hat{c}_l [s]^4 + \hat{c}_r^\dagger \hat{c}_r^\dagger \hat{c}_r \hat{c}_r [a]^4 + (\hat{c}_l^\dagger \hat{c}_l^\dagger \hat{c}_r \hat{c}_r + \hat{c}_l^\dagger \hat{c}_r^\dagger \hat{c}_l \hat{c}_r \\ &\quad + \hat{c}_l^\dagger \hat{c}_r^\dagger \hat{c}_r \hat{c}_l + \hat{c}_r^\dagger \hat{c}_l^\dagger \hat{c}_l \hat{c}_r + \hat{c}_r^\dagger \hat{c}_l^\dagger \hat{c}_r \hat{c}_l + \hat{c}_l^\dagger \hat{c}_r^\dagger \hat{c}_l \hat{c}_l)[s]^2 [a]^2 \\ &\quad + (\hat{c}_l^\dagger \hat{c}_l^\dagger \hat{c}_l \hat{c}_r + \hat{c}_l^\dagger \hat{c}_r^\dagger \hat{c}_l \hat{c}_l + \hat{c}_l^\dagger \hat{c}_r^\dagger \hat{c}_l \hat{c}_l + \hat{c}_r^\dagger \hat{c}_l^\dagger \hat{c}_l \hat{c}_l)[s]^3 [a] \\ &\quad + (\hat{c}_l^\dagger \hat{c}_r^\dagger \hat{c}_r \hat{c}_r + \hat{c}_r^\dagger \hat{c}_l^\dagger \hat{c}_r \hat{c}_r + \hat{c}_r^\dagger \hat{c}_l^\dagger \hat{c}_l \hat{c}_r + \hat{c}_l^\dagger \hat{c}_r^\dagger \hat{c}_r \hat{c}_l)[s][a]^3, \end{aligned} \quad (9)$$

with

$$[s]^i [a]^j = \frac{1}{4} \int d\mathbf{r} (\Phi_g + \Phi_e)^i \cdot (\Phi_g - \Phi_e)^j. \quad (10)$$

After some algebra and using the commutation relations (e.g.  $\hat{c}_r^\dagger \hat{c}_l^\dagger \hat{c}_l \hat{c}_l = \hat{c}_r^\dagger \hat{c}_l \cdot \hat{c}_l^\dagger \hat{c}_l - \hat{c}_r^\dagger \hat{c}_l$ ) we find the two-mode Hamiltonian

$$\hat{H}_{2M} = \frac{E_c}{8} (\hat{c}_r^\dagger \hat{c}_r - \hat{c}_l^\dagger \hat{c}_l)^2 - \frac{E_j}{N} (\hat{c}_l^\dagger \hat{c}_r + \hat{c}_r^\dagger \hat{c}_l) + \frac{\delta E}{4} (\hat{c}_l^\dagger \hat{c}_r + \hat{c}_r^\dagger \hat{c}_l)^2, \quad (11)$$

with the parameters

$$\kappa_{i,j} = \frac{g}{2} \int d\mathbf{r} |\Phi_i|^2 |\Phi_j|^2, \quad (\text{with } i, j = g, e) \quad (12)$$

$$\mu_{g,e} = \int d\mathbf{r} \left( -\frac{\hbar^2}{2m} \Phi_{g,e} \nabla^2 \Phi_{g,e} + \Phi_{g,e} (V_{\text{dw}} + gN |\Phi_{g,e}|^2) \Phi_{g,e} \right), \quad (13)$$

$$E_c = 8\kappa_{g,e}, \quad (14)$$

$$E_j = \frac{N}{2} (\mu_e - \mu_g) - \frac{N(N+1)}{2} (\kappa_{e,e} - \kappa_{g,g}), \quad (15)$$

$$\delta E = \frac{\kappa_{g,g} + \kappa_{e,e} - 2\kappa_{g,e}}{4}. \quad (16)$$

The term proportional to  $E_j$  describes tunnelling of particles from one to the other well, the term proportional to  $E_c$  corresponds to the local interaction within the two wells, and the term proportional to  $\delta E$  takes additional two-particle processes into account. In our experimental parameter range this term is less than  $10^{-5} \times E_j/N$  and less than  $10^{-3} \times E_c/8$  and thus will be neglected for the following discussions. With this, the two-mode Hamiltonian (equation (11)) can be written in the form

$$\hat{H}_{2M} = \frac{E_c}{2} \hat{n}^2 - E_j \hat{\alpha}, \quad (17)$$

with

$$\hat{n} = \frac{\hat{c}_r^\dagger \hat{c}_r - \hat{c}_l^\dagger \hat{c}_l}{2}, \quad \hat{\alpha} = \frac{\hat{c}_r^\dagger \hat{c}_l + \hat{c}_l^\dagger \hat{c}_r}{N}. \quad (18)$$

Here,  $\hat{n}$  is the population imbalance (i.e., atom number difference) operator and  $\hat{\alpha}$  the tunnelling operator. Equation (17) is usually referred to as the Bose–Hubbard Hamiltonian [15, 17–22]. Note that the atom number operator corresponds to the population difference divided by 2. This is due to the fact that the transfer of one particle from one well to the other changes the population difference by two. Furthermore, this definition leads in the Gross–Pitaevskii limit to the canonically conjugate variables  $n$  and  $\phi$  as will be discussed in sections 2.5 and 2.6.

## 2.2. Atom number fluctuations and coherence

Two important properties of the eigenstates of the Bose–Hubbard Hamiltonian are their atom number fluctuations and their coherence. The fluctuation of the atom number difference is defined as

$$\Delta n^2 = \langle \hat{n}^2 \rangle - \langle \hat{n} \rangle^2 = \left\langle \frac{(\hat{c}_r^\dagger \hat{c}_r - \hat{c}_l^\dagger \hat{c}_l)^2}{4} \right\rangle - \left\langle \frac{\hat{c}_r^\dagger \hat{c}_r - \hat{c}_l^\dagger \hat{c}_l}{2} \right\rangle^2, \quad (19)$$

and is a measure for the number of occupied atom number states. Discussions on the state of the BJJ in the Bose–Hubbard picture can be found in [16, 23–27].

The coherence of this many-body system can be quantitatively defined by the first order spatial coherence function  $g^{(1)}(\mathbf{r}, \mathbf{r}')$  as defined in [16]. In the two-mode approximation, it is easy to see from equation (5) that the first order spatial coherence function does not depend on the difference  $(\mathbf{r} - \mathbf{r}')$  and thus is constant in space. With this, the coherence factor  $\alpha$  can be defined in steady state as the uniform value of the spatial coherence function

$$\begin{aligned} \alpha = g^{(1)}(\mathbf{r}, \mathbf{r}') &= \frac{|\langle \hat{\Psi}^\dagger(\mathbf{r}') \hat{\Psi}(\mathbf{r}) \rangle|}{\sqrt{\langle \hat{\Psi}^\dagger(\mathbf{r}') \hat{\Psi}(\mathbf{r}') \rangle \langle \hat{\Psi}^\dagger(\mathbf{r}) \hat{\Psi}(\mathbf{r}) \rangle}} \\ &= \frac{\langle \hat{c}_l^\dagger \hat{c}_r + \hat{c}_r^\dagger \hat{c}_l \rangle}{N} = \frac{\langle \hat{c}_g^\dagger \hat{c}_g - \hat{c}_e^\dagger \hat{c}_e \rangle}{N} = \langle \hat{\alpha} \rangle. \end{aligned} \quad (20)$$

In the two-mode approximation, the coherence factor is directly related to the relative population difference between the ground and the first excited state and corresponds to the expectation value of the tunnelling operator. The eigenstates of the tunnelling operator are the ‘ $SU(2)$  coherent states’ and can be written in the left–right basis as (e.g., from [28–30])

$$|c\rangle = \frac{1}{\sqrt{N! \cdot N^N}} (\psi_l \hat{c}_l^\dagger + \psi_r \hat{c}_r^\dagger)^N |\text{vac}\rangle, \quad (21)$$

where  $\psi_{l,r}$  are complex multipliers and account for the population and the ‘phase’ of the two modes. The state with the highest possible coherence fulfils  $\hat{\alpha}|c\rangle = |c\rangle$  and corresponds to equation (21) with  $\psi_l = \psi_r = \sqrt{N/2}$ . This state is the ground state of the double-well

potential in the non-interacting limit and thus corresponds to totally delocalized particles occupying all the ground state of the potential.

The coherence factor  $\alpha = \langle \hat{\alpha} \rangle$  defined in equation (20) can also be understood as the mean fringe visibility of ensemble-averaged interference patterns which directly corresponds to the averaged momentum distribution. In the steady state the ensemble-averaged momentum distribution is given by

$$\langle \hat{\rho}(\mathbf{k}) \rangle = \frac{N}{2} (|\Phi_g|^2 + |\Phi_e|^2 + \langle \hat{\alpha} \rangle (|\Phi_g|^2 - |\Phi_e|^2)). \quad (22)$$

The equivalence between the coherence factor and the mean fringe visibility can be established by using the approximate momentum distributions for the ground and the first excited state (see figure 3)

$$\Phi_g(\mathbf{k}) \approx f(\mathbf{k}) \cdot \cos(x_0 k_x) \quad (23)$$

$$\Phi_e(\mathbf{k}) \approx f(\mathbf{k}) \cdot i \sin(x_0 k_x), \quad (24)$$

where  $\Phi_g(\mathbf{k})$  and  $\Phi_e(\mathbf{k})$  are the wavefunctions of the ground and the first excited state in momentum space,  $f(k)$  is an envelope function and  $x_0$  is the characteristic distance between the two wells. The resulting momentum distribution is given by

$$\langle \hat{\rho}(\mathbf{k}) \rangle \approx \frac{N|f(\mathbf{k})|^2}{2} (1 + \langle \hat{\alpha} \rangle \cdot \cos(2x_0 k_x + \phi)). \quad (25)$$

Here  $\langle \hat{\alpha} \rangle$  is the amplitude of the modulation of the momentum distribution which is also the visibility of the resulting interference patterns, if the interactions do not perturb the distribution during expansion. A discussion on how interference patterns are measured is given in appendix B.

### 2.3. Rabi, Josephson and Fock regime

The properties of the ground state of the Bose–Hubbard Hamiltonian (equation (11)) depend strongly on the ratio of the local interaction energy and the tunnelling coupling  $E_c/E_j$ . For strong interaction the ground state is localized in the atom number basis (only a few atom number states are populated) and the coherence is low. In the case of strong coupling the coherence is high and the state is delocalized, as shown in figure 1(a), where the coherence (upper graph) and the atom number fluctuations (lower graph) are plotted as a function of  $E_c/E_j$ . Figure 1(b) shows the distribution of atom number states (upper part) and the ensemble-averaged momentum distributions (lower graphs) for three different ratios of  $E_c/E_j$ . It becomes evident that by increasing the ratio  $E_c/E_j$  the atom number fluctuations vanish for  $E_c/E_j > N^{-2}$  before the coherence of the system starts to decrease at  $E_c/E_j > 1$ . By considering this property three regimes can be distinguished, where (1) the coherence is very high and the atom number fluctuations are large, (2) the coherence is high and the atom number fluctuations are small and (3) the coherence is low and the atom number fluctuations vanish. It is convenient to define these three regimes by the ratio of  $E_c/E_j$  [20, 21].

- (1) *Rabi* regime:  $E_c/E_j \ll N^{-2}$ ,
- (2) *Josephson* regime:  $N^{-2} \ll E_c/E_j \ll 1$ ,
- (3) *Fock* regime:  $1 \ll E_c/E_j$ .

The *Rabi* regime corresponds to the non-interacting limit, where the system consists of  $N$  independent particles. The distribution of atom number states is Poissonian and the coherence is very high allowing for the definition of a relative phase between the matter wave packets within the two wells. In the *Josephson* regime the fluctuations of the atom numbers

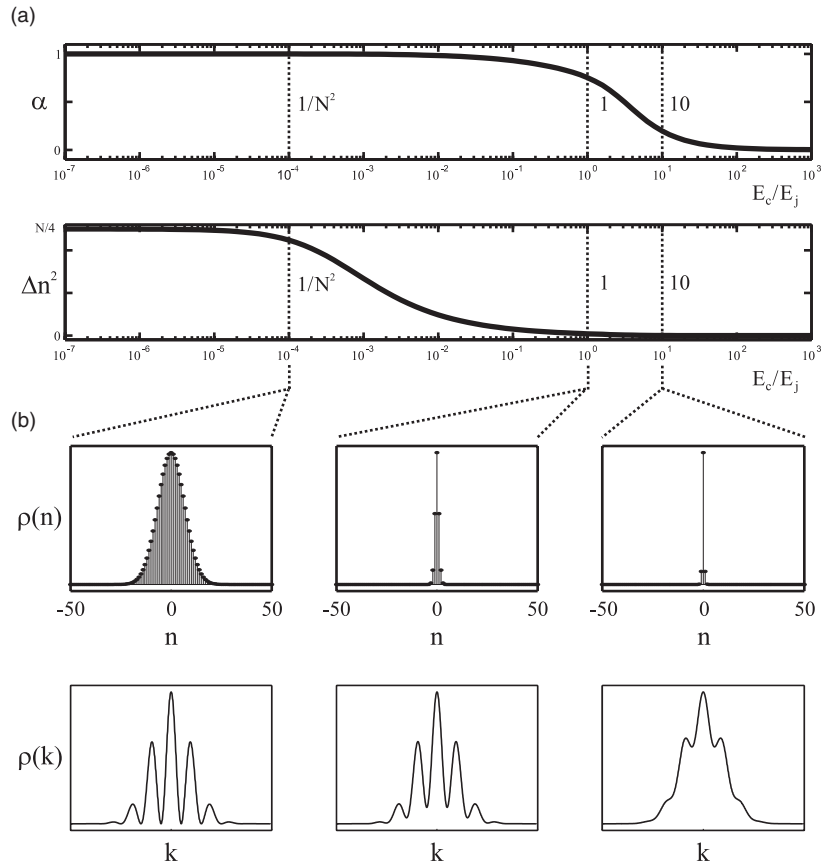


**Figure 1.** Properties of the BJJ for  $N = 100$ . The upper graph in (a) shows the coherence factor  $\alpha$  as a function of  $E_c/E_j$ . The coherence starts to decrease at  $E_c/E_j \gtrsim 1$ . The lower graph is a plot of the population imbalance fluctuations  $\Delta n^2$  as a function of  $E_c/E_j$ . The fluctuations start to decrease at  $E_c/E_j \gtrsim N^{-2}$ . (b) shows the distribution of atom number states (upper part) and the ensemble-averaged momentum distributions (lower graphs) for three different ratios of  $E_c/E_j$ . At  $E_c/E_j = N^{-2}$  the atom number fluctuations are large ( $\Delta n \approx \sqrt{N}/2$ ) and the visibility is almost perfect ( $\alpha \approx 1$ ). Above  $E_c/E_j = 1$  the atom number fluctuations are strongly reduced but the visibility is still high. At  $E_c/E_j = 10$  the atom number fluctuations become very small and the visibility starts to vanish.

are reduced but the coherence is high. Thus, also in this regime a relative phase can be defined, which has only a small quantum mechanical uncertainty. In this regime, for large atom numbers, the operators might be exchanged by complex numbers resulting in a mean-field description of the state. In the *Fock* regime, the Josephson junction is dominated by the interaction energy, therefore the eigenstates have a well-defined atom number in each well and as the coherence vanishes, the phase is completely undefined. In this regime the ground state cannot be described by a single condensate, but corresponds to a fragmented state, where the single-particle density matrix has two macroscopic eigenvalues [31–33].

#### 2.4. Definition of a relative phase

Another experimentally directly accessible quantity is the phase of the interference patterns observed when releasing the atoms from the double-well trap. For each realization perfect

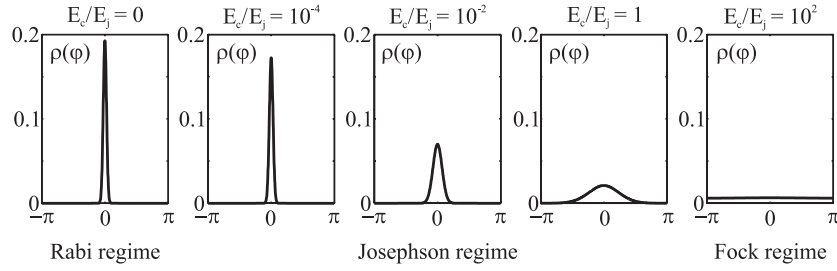


**Figure 2.** Distribution of the relative phases for different ratios of  $E_c/E_j$  for  $N = 100$ . The five graphs show typical distributions of the relative phase for the three regimes, the Rabi regime on the left to the Josephson regime in the centre and the Fock regime on the right. In the Rabi regime the width of the distribution is only determined by the number of particles. In the Josephson regime also the ratio of the interaction energy and the coupling strength plays a role and in the Fock regime the relative phase becomes random.

interference fringes are observed even in the Fock regime but the phase of the patterns is fluctuating from realization to realization as discussed in [34]. Thus, by repeating the experiment many times the distribution function of the phases can be accessed. To be able to make a quantitative comparison of the experimentally obtained phases with the theoretical prediction, a method has to be introduced, how these distribution functions can be extracted from the Bose–Hubbard picture. In the many-body picture it is difficult to define a relative phase operator [35, 36], but as by definition the  $SU(2)$  coherent states have a well-defined relative phase between the two modes. Thus, it is possible to use a projection onto the ‘phase part’ of the  $SU(2)$  coherent states, in order to find the distribution of the relative phases.

An orthonormal phase state basis consists of  $N + 1$  phase states with  $\phi_m = \phi_0 + m \times 2\pi/(N + 1)$  and  $m \in \mathbb{N}$  between 0 and  $N$ :

$$|\phi_m\rangle = \frac{1}{\sqrt{N + 1}} \sum_{n=-N/2}^{N/2} \exp(in\phi_m)|n\rangle. \quad (26)$$

$\phi_0$  is an arbitrary phase and will be set in the following for simplicity to  $-\pi$  leading to the range of relative phases of  $\phi \in [-\pi, \pi]$ .

The phase distribution for any state can be calculated by a projection onto the phase states via  $n(\phi_m) = |\langle\phi_m|\Psi\rangle|^2$ . Typical distributions of the relative phase for the ground state for different  $E_c/E_j$  are shown in figure 2. In steady state the expectation value of  $\hat{\phi}$  is zero and the width of the distribution increases with  $E_c$ . In the Rabi regime  $\Delta\phi$  is small and decreases with the number of particles. In the Fock regime the phase fluctuation increases to its maximal value  $\Delta\phi \lesssim \pi\sqrt{3}$  corresponding to a random distribution and an undefined phase.

### 2.5. Gross–Pitaevskii equation and the two-mode model

With the many-body description it is possible to calculate all relevant quantities and the dynamical response of the BJJ exactly within the two-mode approximation if the spatial wavefunctions  $\Phi_g$  and  $\Phi_e$  are known. In the following we will show that starting from the standard mean-field description of a BEC these wavefunctions can be found. Furthermore, the mean-field picture allows the derivation of a classical Hamiltonian describing the static and dynamic properties of the two conjugate observables, the population imbalance and the relative phase. Since this Hamiltonian also describes the classical motion of a particle in a sinusoidal potential the ongoing physics becomes intuitively accessible.

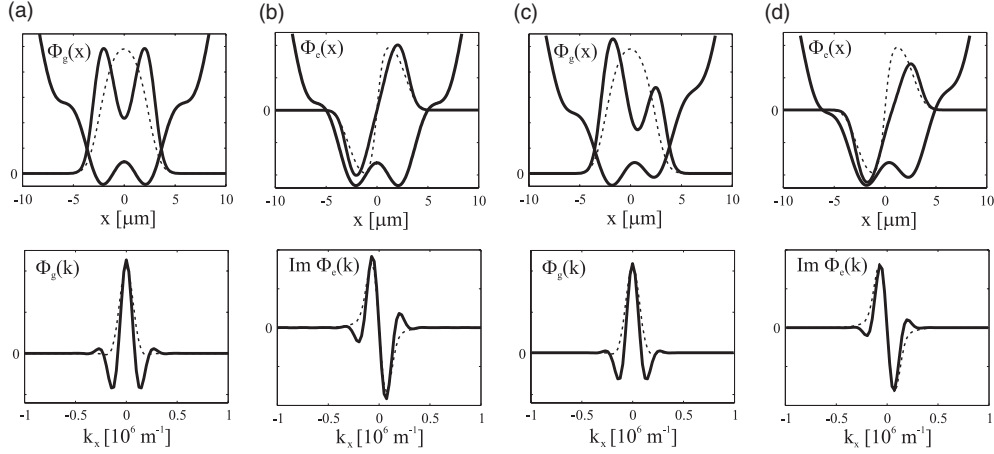


**Figure 3.** First two eigenstates of the double-well potential calculated by solving the Gross–Pitaevskii equation in 3D in a symmetric and an asymmetric potential. The wavefunctions are shown in real space (upper parts) and in momentum space (lower parts) for  $N = 1150$  and  $\omega_x = 2\pi \times 78$  Hz,  $\omega_y = 2\pi \times 90$  Hz,  $\omega_z = 2\pi \times 66$  Hz,  $V_0/h = 420$  Hz,  $|d_{\text{sw}}| = 5.2 \mu\text{m}$ . The asymmetry is generated by moving the periodic potential by  $\Delta x = 500$  nm with respect to the harmonic potential. The solid lines correspond to the ground state wavefunction in the symmetric double-well (a), the first excited state in the symmetric double-well (b), the ground state in the asymmetric double-well (c), and the first excited state in the asymmetric double-well (d). The dashed lines show the corresponding wavefunctions in the harmonic trap at  $V_0 = 0$ .

The many-body Schrödinger equation for a degenerate Bose gas, in the limit of local interaction between the particles, small quantum mechanical uncertainties, and low temperature, can be reduced to the Gross–Pitaevskii equation (GPE)

$$i\hbar \frac{\partial}{\partial t} \Psi(\mathbf{r}, t) = \left( -\frac{\hbar^2}{2m} \nabla^2 + V_{\text{dw}}(\mathbf{r}) + gN_0 |\Psi(\mathbf{r}, t)|^2 \right) \Psi(\mathbf{r}, t)$$

$$\text{with } \int d\mathbf{r} |\Psi(\mathbf{r})|^2 = 1. \quad (27)$$

For low energies, due to the structure of the energy spectrum of the double-well potential, only the first two eigenstates of the GPE can become macroscopically populated, as their energy difference is very small. Thus, the two relevant wavefunctions  $\Phi_g$  and  $\Phi_e$  correspond to these two lowest eigenstates with the chemical potentials  $\mu_{g,e}$

$$\mu_{g,e} \Phi_{g,e}(\mathbf{r}) = \left( -\frac{\hbar^2}{2m} \nabla^2 + V_{\text{ext}}(\mathbf{r}) + gN |\Phi_{g,e}(\mathbf{r})|^2 \right) \Phi_{g,e}(\mathbf{r}). \quad (28)$$

In figures 3(a) and (b) the ground and first excited state wavefunctions in real (upper parts) and momentum space (lower parts) are depicted for characteristic experimental parameters in a symmetric double-well potential. With a coherent superposition of the two wavefunctions in real space it is possible to generate states with any atom number difference, in analogy to the Bose–Hubbard picture. Furthermore, the momentum distribution of the ground state corresponds to an interference pattern at a zero relative phase and the first excited state to a pattern at a  $\pi$  relative phase. Thus, with a coherent superposition of the two states it is also possible to generate interference patterns at all relative phases. Figures 3(c) and (d) depict similar plots for the ground state wavefunction and the first excited state wavefunction in an

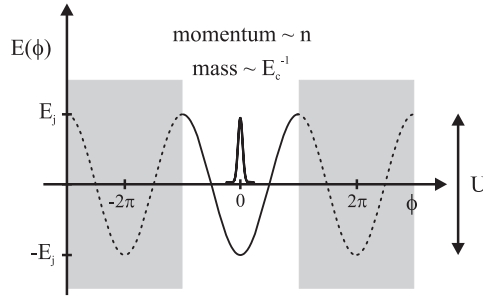


**Figure 4.** Mechanical analogue to the bosonic Josephson junction, a single particle with momentum  $n$  and mass  $E_c^{-1}$  in a sinusoidal potential. The graph shows a sketch of the ground state wavefunction of the single particle in the sinusoidal potential at height  $U$  and a periodicity of  $2\pi$ . The potential is extended beyond the definition of  $\phi \in [-\pi, \pi]$  (dashed line in the grey shaded area).

asymmetric double-well potential. The asymmetry results for both states in a change of the local amplitudes with an increase of the population of the lower well. The wavefunctions in the momentum space are only slightly affected by the asymmetry.

When the two modes are known, the mean-field description can be used in order to gain intuitive insight into the properties and the behaviour of the BJJ. The Hamiltonian in the mean-field picture can be derived by substituting the creation and annihilation operators into the two-mode Hamiltonian equation (5) by complex numbers (e.g.,  $\hat{c}_l \Rightarrow \sqrt{N_l(t)} e^{i\phi_l(t)}$ ). If  $\delta E$  is negligible, which is the case for our experimental situation, then the Gross–Pitaevskii two-mode Hamiltonian has the form

$$H_{\text{GP-2M}} = \frac{E_c}{2} n^2 - E_j \sqrt{1 - \frac{4n^2}{N^2}} \cos \phi, \quad (29)$$

with

$$n = \frac{N_l - N_r}{2}, \quad \phi = \phi_r - \phi_l. \quad (30)$$

Here  $n$  is the population imbalance divided by 2 and  $\phi$  the relative phase between the wavefunction in the right and the left well.

## 2.6. Mechanical analogue—a simple picture

The already mentioned analogy of a BJJ with a particle in a sinusoidal potential becomes obvious by associating the population difference with the momentum of a particle  $n \Leftrightarrow p$  which has a mass of  $m = 1/E_c$  and the relative phase with the position of the particle  $\phi \Leftrightarrow x$ . With that, as depicted in figure 4, the tunnelling coupling  $E_j$  defines the height  $U$  of the sinusoidal potential. It is important to note that the absolute height decreases with increasing momentum  $U = 2E_j \sqrt{1 - \frac{4n^2}{N^2}}$ .

As an instructive example we will show that the quantum mechanical uncertainties  $\Delta x^2$ ,  $\Delta p^2$  associated with the ground state of the particle in the sinusoidal potential are equal to the atom number and phase uncertainties derived within the Bose–Hubbard model. However, it is important to note that the phase in this context is only meaningful, if the phase distribution is sharply peaked around a mean value. This is the case in the Rabi or the Josephson regime. In the Fock regime a mean phase cannot be defined and thus the following discussion is not

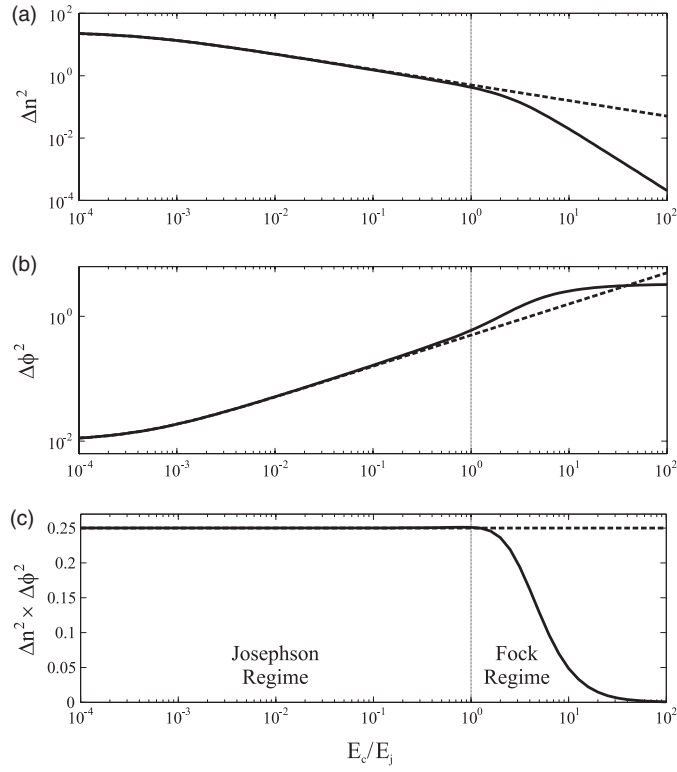


**Figure 5.** Comparison of the uncertainties of the variables  $n$  and  $\phi$  according to the Bose–Hubbard model (solid line) and the simple mechanical analogue (dashed line). (a) Phase fluctuations, (b) the atom number fluctuations and (c) the product of the two uncertainties revealing that  $\phi$  and  $n$  are conjugate variables in the Rabi and Josephson regime. In the Fock regime the atom number fluctuations are smaller than expected and the phase fluctuations are bound leading to a strong deviation of the product from the expectation due to the mean-field model.

adequate. By expanding the Hamiltonian to second order in  $\phi$  and  $n$  we obtain

$$H_{\text{simplified}} = \left( E_c + \frac{4E_j}{N^2} \right) \frac{n^2}{2} + \frac{E_j}{2} \phi^2, \quad (31)$$

which describes a single particle in a harmonic potential with the standard quantum mechanical uncertainties of the ground state leading to (e.g. [37])

$$\Delta p^2 \Leftrightarrow \Delta n^2 = \frac{1}{2} \sqrt{\frac{E_j}{E_c + 4E_j/N^2}}, \quad \Delta x^2 \Leftrightarrow \Delta \phi^2 = \frac{1}{2} \sqrt{\frac{E_c + 4E_j/N^2}{E_j}}. \quad (32)$$

The product of the fluctuations of the two dynamical variables  $n$  and  $\phi$  as a function of the system parameters  $E_c$  and  $E_j$  leads to an uncertainty relation of the form

$$\Delta n^2 \times \Delta \phi^2 \geq 1/4, \quad (33)$$

where the equality is valid for the ground state. The comparison of this uncertainty relation with the calculation using the Bose–Hubbard model is shown in figure 5. The solid lines were calculated with the Bose–Hubbard model with  $N = 100$  and the dashed lines are the prediction of the GP two-mode model. In the Rabi and Josephson regime the agreement is excellent as in

these regimes the mean-field description is adequate; however in the Fock regime the product vanishes, as the fluctuation of the atom numbers becomes arbitrarily small but the fluctuation of the phase is bound between 0 and  $\pi$ .

### 3. Steady state properties at zero temperature

At zero temperature in a symmetric double-well potential the expectation values of the population imbalance and the relative phase vanish. The mean-field ground state of the BJJ is characterized by a uniform phase and thus the relative phase between the two wells in the steady state is always zero. However, by introducing an energy asymmetry between the two wells, the ground state population imbalance can be modified.

For the double-well potential defined in equation (1), which consists of a harmonic trapping potential and a periodic potential, an asymmetry can be introduced by changing the position of the harmonic trap. A shift of  $\Delta x$  leads to the potential

$$\begin{aligned} V_{\text{dw}}^{\text{asymm}} &= \frac{1}{2}m(\omega_x^2(x - \Delta x)^2 + \omega_y^2y^2 + \omega_z^2z^2) + \frac{V_0}{2} \left(1 + \cos \frac{2\pi}{d_{\text{sw}}}x\right) \\ &= V_{\text{dw}} - m\omega_x^2x\Delta x + \text{const}, \end{aligned} \quad (34)$$

where the shift is equivalent to an additional potential gradient. The resulting Bose–Hubbard Hamiltonian for the asymmetric double-well potential has the form

$$\begin{aligned} \hat{H}_{2M}^{\text{asymm}} &= \hat{H}_{2M} - \Delta x \cdot \delta \cdot \left( \frac{\hat{c}_r^\dagger \hat{c}_r - \hat{c}_l^\dagger \hat{c}_l}{2} \right) \\ &= \frac{E_c}{2} \hat{n}^2 - \Delta x \cdot \delta \cdot \hat{n} - E_j \hat{\alpha} \\ &= \frac{E_c}{2} \left( \hat{n} - \frac{\Delta x \cdot \delta}{E_c} \right)^2 - E_j \hat{\alpha} + \text{const}, \end{aligned} \quad (35)$$

with the coupling constant

$$\delta = 2m\omega_x^2 \int \mathbf{dr} \Phi_s^* x \Phi_a. \quad (36)$$

From equation (35) it follows that the ground state in the asymmetric double-well trap has a population imbalance of  $\Delta n_0 = \Delta x \cdot \delta / E_c$ . The distribution of the relative phases remains unchanged in the asymmetric double-well potential, however the coherence is reduced, as  $\langle \hat{\alpha} \rangle$  corresponds to the visibility of averaged interference patterns and their visibility depends on the relative amplitudes of the two interfering modes.

In the Gross–Pitaevskii model a similar term appears as

$$H_{\text{GP-asymm}} = E_c \frac{n^2}{2} - E_j \sqrt{1 - \frac{4n^2}{N^2}} \cos \phi - \delta \cdot \Delta x \cdot n, \quad (37)$$

leading to the same predictions for the ground state population imbalance.

To measure the ground state population imbalance experimentally we prepare a BEC in the ground state of an asymmetric double-well potential. The asymmetry is experimentally realized by changing the position of the harmonic trapping potential with respect to the standing light wave. The details of the experimental setup and the generation of the double-well potential can be found in appendix A.

The initial state of the BJJ is prepared by condensing  $1450 \pm 250$  atoms in a 3D harmonic trapping potential with trapping frequencies  $\omega_x = 2\pi \times 78(1)$  Hz,  $\omega_y = 2\pi \times 66(1)$  Hz and  $\omega_z = 2\pi \times 90(1)$  Hz. To prepare the BJJ adiabatically the standing light wave with periodicity

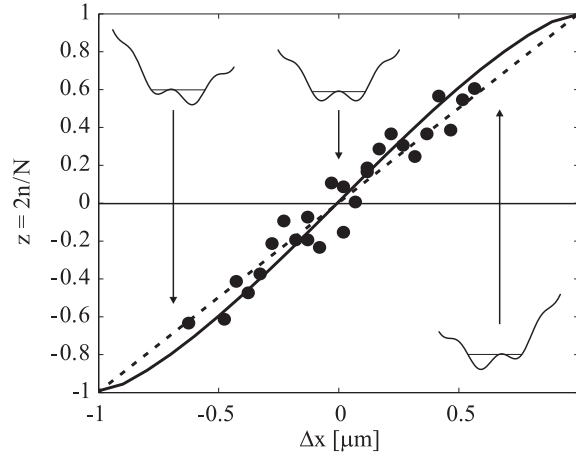


**Figure 6.** Steady state population imbalance as a function of the shift of the harmonic trapping potential. The solid line is the solution of the 3D Gross–Pitaevskii equation and the dashed line is the prediction of the Bose–Hubbard model.

$d_{sw} = 5.2(2) \mu\text{m}$  is raised within 1s to a height of 580(10) Hz. The tunnelling coupling, the charging energy and the energy shift are calculated by solving the Gross–Pitaevskii equation in 3D and are  $E_j/h = 1.17$  kHz,  $E_c/h = 0.32$  Hz, and  $\delta/h = 231$  Hz  $\mu\text{m}^{-1}$ .

The experimentally found steady state population imbalances are plotted as a function of the shift of the harmonic trapping potential in figure 6. The solid line is the solution of the 3D Gross–Pitaevskii equation and the dashed line is the prediction of the Bose–Hubbard model. The data area in good agreement with both theoretical predictions within the experimental error. The discrepancy between the Bose–Hubbard and the full Gross–Pitaevskii model results from the fact that the asymmetry changes the wavefunctions of the ground and excited state which is not taken into account in the framework of the employed simple two-mode approximation.

#### 4. Steady state properties at finite temperature

At finite temperature the fluctuation of the dynamical variables are larger than the corresponding quantum mechanical uncertainties. The reason for these thermally induced fluctuations is the equilibration of the bosonic Josephson junction with its thermal environment. According to the Bose–Einstein distribution in the double-well potential not only the ground state but also the first excited state will be macroscopically populated, if their energy difference is smaller than the thermal energy scale. To calculate the effect of the temperature we neglect the back action of the thermal excitations on the mean-field wavefunctions and the exchange of particles. Thus, the interaction of the BJJ with its thermal background is only via a transfer of energy.

The density matrix of the mixed state at finite temperature can be calculated in the eigenstate basis by populating the eigenstates according to the Boltzmann distribution

$$\hat{\rho}_{\text{th}} = \frac{1}{C} \sum_{e=0}^N \exp\left(-\frac{\langle e|\hat{H}|e\rangle}{k_B T}\right) |e\rangle\langle e|, \quad (38)$$

where  $|e\rangle$  are the  $N + 1$  eigenstates of the Hamiltonian,  $k_B$  is the Boltzmann constant and  $C$  is a normalization constant.

The coherence factor  $\alpha = \langle \hat{\alpha} \rangle = \text{Tr}(\hat{\rho}_{\text{th}} \hat{\alpha})$  defined in equation (20) also at finite temperature in the steady state is a good measure for the coherence of the system and is connected to the amount of phase fluctuations in general. For temperatures much higher than the mean quantum mechanical level spacing, which is approximately given at low energy by the plasma energy

$$\hbar\omega_p = \sqrt{E_j \left( E_c + \frac{4E_j}{N^2} \right)} \quad (39)$$

a semi-classical calculation of the thermally averaged fringe visibility is appropriate. In this limit the many-body two-mode Hamiltonian (equation (17)) corresponds to the classical Hamilton function (equation (29)) and the coherence factor is the mean value of  $\cos \phi$  which writes

$$\langle \cos \phi \rangle = \frac{\int dn d\phi \cos \phi \exp(-H_{GP-2M}/k_B T)}{\int dn d\phi \exp(-H_{GP-2M}/k_B T)}. \quad (40)$$

In the Josephson regime, the relatively strong interaction term  $E_c$  makes at finite temperature the population of large  $n$  energetically unfavourable. The coherence factor can then be approximated by ([37])

$$\alpha = \langle \cos \phi \rangle = \frac{\int d\phi \cos \phi \exp\left(-\frac{E_j}{k_B T} \cos \phi\right)}{\int d\phi \exp\left(-\frac{E_j}{k_B T} \cos \phi\right)} = \frac{I_1\left(\frac{E_j}{k_B T}\right)}{I_0\left(\frac{E_j}{k_B T}\right)}, \quad (41)$$

where  $I_i(j)$  are the modified Bessel functions of the first kind. At high temperatures, the agreement between this analytic expression and the prediction of the Bose–Hubbard model is always very good (see figure 8).

The magnitude of the thermally induced fluctuations can also be directly deduced from the mechanical analogue as long as the phase fluctuations are smaller than  $\Delta\phi \ll \pi$  by using the simplified Hamilton function (equation (31)), and assuming the Boltzmann distribution leading to the fluctuations

$$\Delta n_{\text{th}}^2 = \frac{k_B T}{E_c + \frac{4E_j}{N^2}}, \quad \Delta\phi_{\text{th}}^2 = \frac{k_B T}{E_j}. \quad (42)$$

The product of the thermally induced fluctuation of the population imbalance and the phase gives also rise to an ‘uncertainty relation’ of the form

$$\Delta n_{\text{th}}^2 \times \Delta\phi_{\text{th}}^2 \geq \frac{(k_B T)^2}{E_j \left( E_c + \frac{4E_j}{N^2} \right)} = \left( \frac{k_B T}{\hbar\omega_p} \right)^2. \quad (43)$$

To experimentally investigate the amount of thermal fluctuations in the BJJ, the distribution of the relative phase for many realizations is measured as a function of the temperature, the barrier height and the atom numbers [38]. The experiments are performed by condensing about 2000 to 10 000 atoms in the 3D harmonic trap with trapping frequencies  $\omega_x = 2\pi \times 90(2)$  Hz and  $\omega_{y,z} = 2\pi \times 100(2)$  Hz at the lowest possible temperature of about 10 nK. Then the temperature is increased by keeping the atoms in the harmonic trap for different holding times, where due to uncontrolled fluctuations of the trap parameters energy is transferred to the atoms. For these experiments it is crucial that the temperature can be deduced independently, thus the adjusted temperature is in the range of 50–80 nK, which can be accurately measured by standard thermometry methods. The atom number of the initial condensate is chosen such that after the heating process the number of the condensed particles stays in the range of 1900 and 3600 atoms.

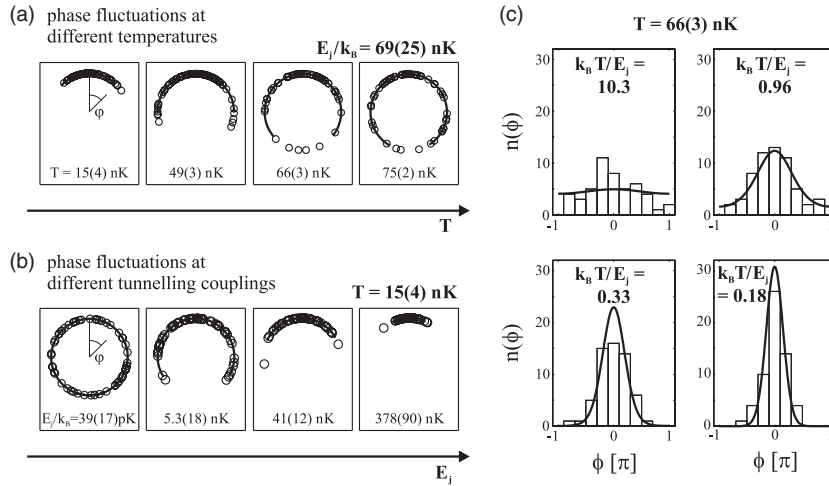


**Figure 7.** Thermally induced fluctuations. (a) shows polar plots of relative phase measurements for a fixed barrier height leading to a constant tunnelling coupling and for different temperatures. Every open circle corresponds to a single realization of the interference measurement. The solid line shows twice the standard deviation of the phase. The amount of fluctuations increases with temperature. (b) corresponds to similar experiments, but here the temperature is fixed and the barrier height varied in order to realize different tunnelling couplings. (c) shows phase distributions for different ratios of the temperature and the tunnelling coupling. The solid line represents the classical prediction taking also into account the experimental uncertainty of the deduced phase.

Once the Bose gas is prepared in the 3D harmonic trap the standing light wave with a periodicity of  $d_{sw} = 4.8(2) \mu\text{m}$  is raised within 300 ms to its final value of between  $V_0/h = 500$  Hz and 2000 Hz. The resulting coupling constants are  $E_j/k_B$  between 1.6 nK and 640 nK and  $E_c/k_B$  between 13 pK and 21 pK. The plasma energy ranges between  $\hbar\omega_p/k_B = 0.1$  nK and 4 nK and the tunnelling times between  $\tau_p = 12$  ms and 500 ms. After the ramp all potentials are turned off within 200  $\mu\text{s}$  and the resulting interference patterns imaged after 5 or 6 ms time of flight.

The qualitative analysis of the phase fluctuations is shown in figure 7, where polar diagrams of relative phase measurements are plotted. Every open circle corresponds to a single interference experiment and the solid lines show twice the standard deviation. In (a) the barrier height is kept constant leading to a tunnelling coupling of  $E_j/k_B T = 69(25)$  nK and the temperature is varied between  $T = 15(4)$  nK and 75(2) nK. The fluctuations clearly increase with temperature. In (b) the temperature is kept constant at  $T = 15(4)$  nK and the barrier height changed leading to a tunnelling coupling between  $E_j/k_B T = 39(17)$  pK and 378(90) nK. Here the fluctuations decrease with increasing coupling. Four distribution functions for different ratios of the thermal energy and the tunnelling coupling are shown in (c) in form of histograms. The classical expectation (solid line) is in good agreement with the experimental findings, when also the experimental uncertainty of the phase deduction is taken into account.

The measured coherence factors  $\alpha$  as a function of the scaling parameter  $k_B T/E_j$  are shown in figure 8. Here for every temperature and barrier height about 100 measurements are performed and every data point in the graph corresponds to a subset extracted from these measurements for different atom number ranges (e.g., 2000 to 2500, 2500 to 3000 etc atoms in the condensate fraction). Each data point represents at least 28 and on average 40 measurements. The coherence factor is calculated by averaging over the cosine of the fitted

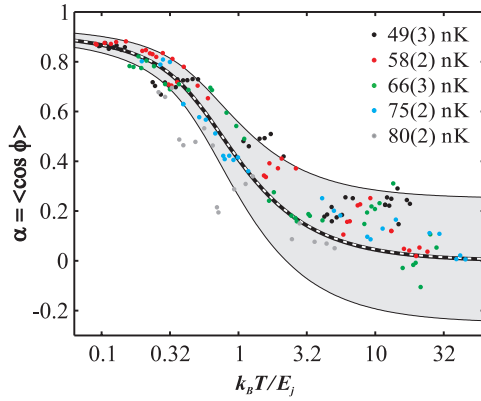


**Figure 8.** Experimental investigation of the coherence factor  $\alpha$  as a function of the scaling parameter  $k_B T / E_j$ . Each data point corresponds to the average of at least 28 (typically about 40) single measurements for different  $T$  and  $E_j$ . The temperature is measured independently with a time-of-flight method and the coupling strength is deduced from 3D simulations of the BJJ using the independently measured system parameters (potential parameters and atom numbers). The experimental error of  $k_B T / E_j$  is about  $\pm 30\%$ . The central black line corresponds to the prediction of the Bose–Hubbard theory and the white dashed line is the prediction of the classical theory, where both calculations take the uncertainty of the phase fitting into account. The grey shaded area shows twice the expected standard deviation of the coherence factor due to the finite number of measurements. The behaviour of the coherence factor is confirmed over a three orders of magnitude change of the scaling parameter.

phases. The Josephson energy  $E_j$  is deduced for every point at the given trap parameters and the mean atom numbers in the condensate fraction by numerically solving the Gross–Pitaevskii equation in 3D.

The shown behaviour is in quantitative agreement with the prediction of the classical model (white dashed line) since for the accessible parameter range the quantum fluctuations are very small

$$\Delta\phi_{\text{th}}^2 = \frac{k_B T}{E_j} \gg \Delta\phi_{\text{qm}}^2 = \frac{1}{2} \sqrt{\frac{(E_c + 4E_j/N^2)}{E_j}} \Rightarrow k_B T \gg \frac{\hbar}{2} \omega_p. \quad (44)$$

In the experimentally accessible regime quantum mechanical fluctuations are negligible as  $k_B T / \hbar \omega_p > 10$ .

The temperature for every data point is deduced from three different quantities. In the single interference images the thermal background can be fitted transversally to the interference patterns with a Gaussian function and the temperature might thus be deduced from the size of the thermal cloud. Additionally, independent time-of-flight measurements are performed releasing the atoms from the harmonic trap. Here, the temperature is deduced from both the expansion velocity of the thermal cloud and the ratio of the condensed and the thermal fraction. All three methods lead within the experimental error to the same results. The last method leads to the smallest fitting uncertainty and thus is chosen for calculating  $k_B T / E_j$  in figure 8.

The typical error of  $k_B T / E_j$  is  $\pm 30\%$ . The error in  $E_j$  results from the uncertainty of the atom numbers, the trapping frequencies, the barrier height and the lattice spacing of the periodic potential. The error in  $T$  results from the fitting error of the waists and amplitudes of the double Gaussian distribution of the independent time-of-flight measurements.

The central black line in figure 8 shows the theoretical prediction of the Bose–Hubbard model for the coherence factor and the white dashed line is the classical prediction in the high temperature limit. The fitting error of the relative phases is taken into account for the calculation of both theory curves. The influence of the fitting error on the coherence factor is estimated by averaging over an additional fluctuating phase with a box shaped distribution function with a standard deviation corresponding to the fitting error. For our experiments the fitting error of the relative phase is  $0.13\pi$  and leads to a reduction of the coherence factor of  $\alpha' = 0.92\alpha$ . The grey shaded area shows twice the standard deviation of the coherence factor resulting from the finite number of measurements, which is for about 40 measurements approximately  $\Delta\alpha \approx 0.13 \times (1 - \alpha)$ .

The dependence of the coherence factor on  $T$  and  $E_j$  is consistent with the prediction of the two-mode model over a wide range. For small values of  $k_B T/E_j$  the coherence factor is in close agreement with the theoretical prediction. However, for  $k_B T/E_j > 2$  the data points lie within the experimental error but are mainly localized above the curve. This deviation can be explained by the fact that the BJJ is not thermalized for small  $E_j$  (see appendix C). The points corresponding to a high temperature of 80 nK lie outside the shaded region revealing a lower degree of coherence. A disagreement in this regime can also be expected as the temperature is close to the critical temperature of  $T_c \approx 87$  nK. The analogy with superconducting Josephson junctions where a deviation close to  $T_c$  has been predicted [39], is under investigation.

The classical phase fluctuations are of fundamental interest however, the successful demonstration opens up the route for applying these measurements for thermometry in the ultralow temperature regime, where standard techniques fail. More details are discussed in appendix C.

## 5. Dynamical properties of the bosonic Josephson junction

The dynamical response of the bosonic Josephson junction to low energetic excitation can be calculated in the many-body two-mode description. The temporal evolution of the wavefunction is governed by the temporal propagation of the density matrix

$$\hat{\rho}(t) = e^{-i\hat{H}t/\hbar} \hat{\rho}(t=0) e^{i\hat{H}t/\hbar} \quad \text{with} \quad \hat{\rho} = |\hat{\Psi}\rangle\langle\hat{\Psi}|. \quad (45)$$

In the eigenbasis the time propagation operator corresponds to a phase evolution of the eigenstates according to their energy. With this, the expected dynamical behaviour of the BJJ in the three dynamical regimes can be understood by the structure of the energy spectrum and the eigenstate wavefunctions. In figure 9 the eigenstates and the eigenenergies of the Bose–Hubbard Hamiltonian for  $N = 100$  are shown in the Rabi regime (a), in the Josephson regime (b) and in the Fock regime (c). The eigenstates in the Rabi regime are the  $SU(2)$  coherent states and show a linear, harmonic oscillator like energy spectrum. In the Fock regime the eigenstates are localized atom number states and the energy spectrum is similar to the energy spectrum of a free particle. In the Josephson regime for low energies  $E < 2E_j$  the eigenstates are similar to coherent states with a well-defined phase and for large energies  $E > 2E_j$  they are similar to Fock states with a well-defined atom number.

In the Rabi regime the eigenstate wavefunctions and the energy spectrum is similar to a harmonic oscillator and thus the dynamical response to low energetic excitations are harmonic, plasma oscillations. In the Fock regime the eigenstates are localized in the Fock space and every energy (except of the ground state at an even number of particles) is a doublet with a quasi-degenerate symmetric and an antisymmetric state. The preparation of a single Fock state, corresponding to a population imbalance, consists of the superposition of two degenerate states and will show no (or only an extremely slow) temporal evolution. The preparation of

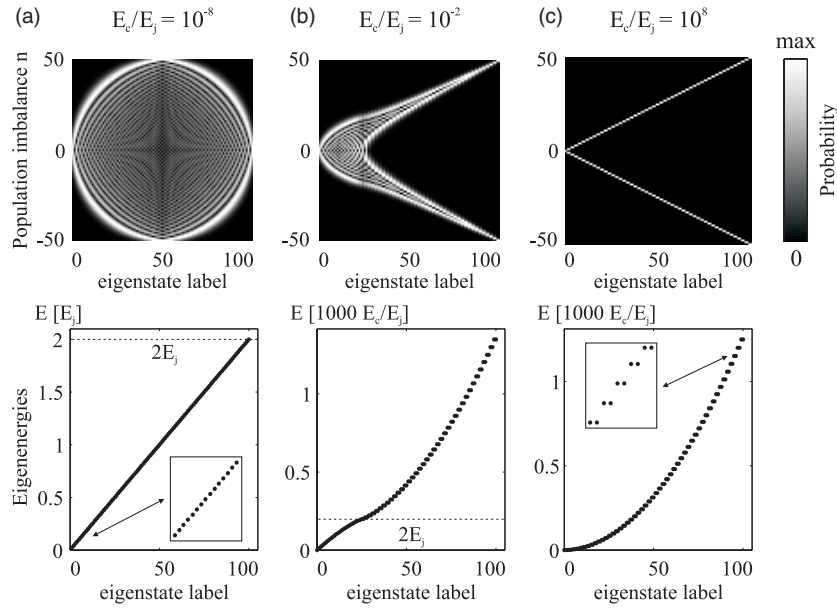


**Figure 9.** Eigenstates and energy spectra of the Bose–Hubbard Hamiltonian in the three dynamical regimes. (a) shows the coherent eigenstates in the Rabi regime, which are strongly delocalized. The energy scale is only given by the tunnelling coupling and the eigenenergies increase linearly with the eigenstate label. (b) corresponds to the Josephson regime, where the low lying excitations are delocalized and coherent and the higher excitations are well localized atom number states. In (c) the eigenstates in the Fock regime are shown. The strong localization is evident and the energy, which is dominated by the interaction energy, shows a quadratic increase. Every eigenenergy is two-fold degenerate and corresponds to well-defined atom number states at  $n$  and  $-n$ .

many Fock states thus will keep the mean population imbalance constant, as the doublets are not evolving, but the energy difference between the doublets will lead to a rapid oscillation on top. The dynamics in the Josephson regime depends on the exact preparation of the initial state. For low energetic excitations ( $E < 2E_j$ ) the BJJ shows plasma oscillations and for high energetic excitations ( $E > 2E_j$ ) self-trapping.

Furthermore, in the context of the Bose–Hubbard model, additional dynamical effects exist, which are not connected to the mean values of the population imbalance and the relative phase but to their fluctuations. If not an initial imbalance is prepared but the coupling constants are changed in time, then phenomena such as collapses and revivals are anticipated. More detailed discussions on this topic can be found in [16, 40–43].

However, for a quantitative understanding of the dynamical response in the Bose–Hubbard picture the temporal evolution has to be calculated numerically. Intuitive insight can be won by considering the Gross–Pitaevskii two-mode description and calculating the equation of motion for  $n$  and  $\phi$  [15, 18, 22, 44–49]

$$\frac{dn}{dt} = -\frac{1}{\hbar} \frac{\partial H}{\partial \phi} = -\frac{E_j}{\hbar} \sqrt{1 - \frac{4n^2}{N^2}} \sin \phi, \quad (46)$$

$$\frac{d\phi}{dt} = \frac{1}{\hbar} \frac{\partial H}{\partial n} = \frac{E_c}{\hbar} n + \frac{E_j}{\hbar} \frac{4n}{N^2} \left( \sqrt{1 - \frac{4n^2}{N^2}} \right)^{-1} \cos(\phi). \quad (47)$$

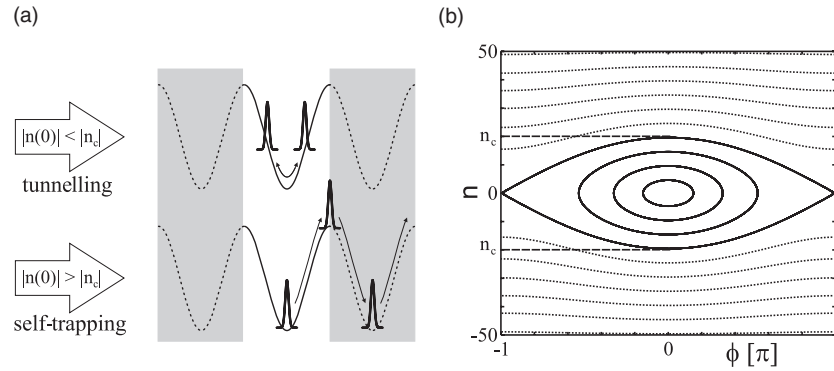


**Figure 10.** Dynamics of the bosonic Josephson junction. In (a) the two expected dynamical regimes are shown. The upper graph corresponds to an initial kick, which is smaller than a critical value, leading to oscillations of the particle around its equilibrium position, i.e. plasma oscillations. If the kick is large enough such that the particle can reach the potential maxima as shown in the lower graph, it will continue moving through the periodic potential. The particle is in the self-trapping regime. The corresponding phase plane portrait is shown in (b), where the ellipsoids depict the plasma oscillation modes and the dotted lines the self-trapped modes. The separatrix divides the phase plane into the two regimes.

The experimentally accessible dynamical modes become obvious employing the mechanical analogue, i.e. solving the equation of motion by intuition. If the particle is slightly moved away from its ground state position (i.e., a small phase is imprinted) or the particle has a small initial kick (i.e., a small initial population imbalance) as sketched in the upper graph in figure 10(a), then the particle will perform harmonic oscillations around the minimum of the potential at the characteristic plasma frequency

$$\omega_p = \frac{1}{\hbar} \sqrt{E_j \left( E_c + \frac{4E_j}{N^2} \right)}. \quad (48)$$

The oscillations of the particle correspond to oscillation of the population imbalance and the relative phase around a zero mean value, and the BJJ is in the plasma oscillation regime.

For larger momenta the assumption for the derivation of the simplified Hamilton function (equation (31)) are not fulfilled and the full two-mode Hamilton function (equation (29)) should be considered instead. If the initial kick is large enough such that the particle can reach the top of the potential as shown in the lower graph in figure 10(a), then the particle will continue moving through the periodic potential. In this case the position coordinate will increase in time and the momentum will always point into the same direction leading to a non-zero mean value. This corresponds in the BJJ to the winding up of the relative phase and a non-vanishing mean population imbalance. With this, the BJJ is in the self-trapping regime. The condition for self-trapping is, that the initial energy of the particle is just enough to reach the top of the potential (i.e.,  $\phi = \pi$  at  $n = 0$ ), which is the case if  $H(n_c, \phi = 0) > H(n = 0, \phi = \pi)$ . Thus, the critical initial imbalance  $n_c$  for a zero initial phase difference is defined as

$$\frac{E_c}{2} n_c^2 - E_j \sqrt{1 - \frac{4n_c^2}{N^2}} = E_j \Rightarrow |n_c| = 2 \sqrt{\frac{E_j}{E_c} \left( 1 - \frac{4E_j}{N^2 E_c} \right)}. \quad (49)$$

A discussion on the optimal conditions for observing the Josephson dynamics can be found in [50].

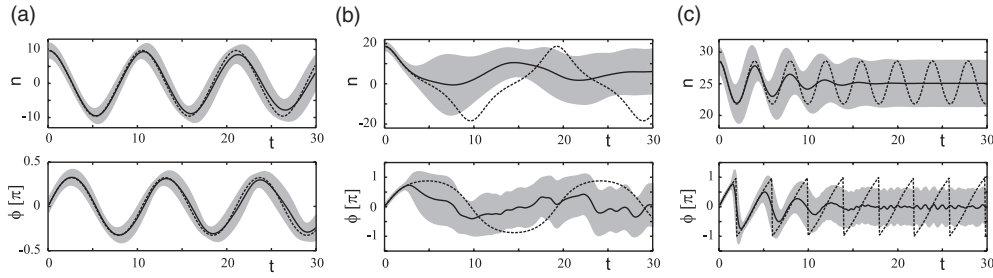


**Figure 11.** Dynamics of the bosonic Josephson junction at  $N = 100$  and  $E_c/E_j = 0.01$ . The graphs show the temporal evolution of the dynamical variables  $n$  (upper graphs) and  $\phi$  (lower graphs) calculated with the GP model (dotted lines) and the many-body model (solid lines), where the grey shaded area corresponds to plus/minus the fluctuations of the respective quantities. (a) is initiated by a population imbalance of  $n(0) = 9.6$  and shows the dynamics in the plasma oscillation regime. In (b) the dynamics starts with a population imbalance of  $n(0) = 19.2$ , which is slightly below the critical population imbalance of  $n_c = 19.6$ . (c) shows the response of the system, when the initial population imbalance is  $n(0) = 28.7$  and reveals self-trapping.

Also a third dynamical regime exists due to the momentum dependence of the potential height leading in certain cases to stable oscillations around the top of the potential. For details on this regime we refer to [46].

The dynamical response of the bosonic Josephson junction can be visualized in the phase plane portrait, where the population imbalance is plotted versus the relative phase (modulo  $2\pi$ ). A typical phase plane portrait is shown in figure 10(b) for  $N = 100$  and  $E_c/E_j = 0.01$  (Josephson regime). In the central part of the graph the periodic (plasma) oscillations in the zero-phase regime are indicated by ellipsoids. Above and below the self-trapped states are plotted. The two regimes are separated by the separatrix, which is characterized by the initial condition  $n_0 = \pm n_c$  at  $\phi_0 = 0$ .

Figure 11 shows the comparison of the predictions of the equations of motion (solution of equations (46) and (47), dashed lines) and the numeric simulations of the many-body system (solid lines) for  $N = 100$  and  $E_c/E_j = 0.01$ . The grey shaded areas correspond to plus/minus the expectation value of the fluctuation operators of the respective quantities. In the upper graphs the temporal evolution of the population imbalance is plotted and in the lower graphs the temporal evolution of the relative phase. For the three graphs different initial conditions are prepared, by starting with the ground state of different asymmetric double-well potentials leading to the initial population differences of  $n(0) = 9.6$  (a), 19.2 (b) and 28.7 (c). The dynamics is initiated, when the energy asymmetry is lifted.

In the zero-phase mode regime (figure 11(a)) the GP prediction is in good agreement with the many-body calculation. A small reduction of the oscillation amplitude in the many-body case can be found for long oscillation times. In the case of self-trapping (figure 11(c)) the GP prediction is in good agreement with the many-body calculation for short times, but the oscillations disappear rapidly due to a dephasing of the populated atom number states. Close to the separatrix (figure 11(b)) the GP prediction is only valid for a very short time. It starts to deviate strongly from the many-body description, when the relative phase approaches  $\pi$ . This is due to the fact that in the many-body case not only a single Fock state but many atom number states are populated. Thus, at the critical population imbalance there are states which are self-trapped but also states which are not. By increasing the number of particles the deviations become less relevant and the classical equations can be used to predict the behaviour of the BJJ also for longer times.

The possibility of generating a tunnel array for Bose–Einstein condensates was demonstrated in 1998 by M A Kasevich and coworkers [51]. In these experiments a BEC was trapped in a vertically oriented periodic potential and atoms were coupled out due to the influence of gravity. The experiments showed that if the matter wave packets within the lattice have initially a constant phase relation from well to well, the out-coupled probability distribution is periodically modulated due to matter wave interference and if the phases are random initially the probability distribution will be constant.

Later, in 2001, also the Josephson dynamics was observed with Josephson junction arrays [52]. In the following discussion however, we will focus on the experimental investigation of the dynamics of a *single* bosonic Josephson junction, which was produced for the first time in 2005 [53].

The initial state of the BJJ is prepared by condensing 1150 atoms (where the number of atoms is fixed by post selection to be between 1000 and 1300) at a temperature below 20 nK in a 3D harmonic trapping potential with trapping frequencies  $\omega_x = 2\pi \times 78(1)$  Hz,  $\omega_y = 2\pi \times 66(1)$  Hz and  $\omega_z = 2\pi \times 90(1)$  Hz. To prepare the BJJ adiabatically the standing light wave with periodicity  $d_{sw} = 5.2(2)$   $\mu\text{m}$  is raised within 1s to a height of 420(5) Hz<sup>1</sup>. The tunnelling coupling, the charging energy and the energy shift are calculated by solving the Gross–Pitaevskii equation in 3D and are  $E_j/h = 3.15$  kHz,  $E_c/h = 0.33$  Hz,  $\delta E/h = 0.14$  mHz and  $\delta/h = 204$  Hz  $\mu\text{m}^{-1}$  leading to the plasma frequency  $\omega_p = 2\pi \times 33$  Hz. The resulting thermally induced fluctuations of the dynamical variables are  $\Delta\phi_{th} = 0.1\pi$  and  $\Delta n_{th} = 36$ , which are small compared to the change of the dynamical variables during the evolution and thus lead only to a small uncertainty of the initial conditions. It is important to note that the uncertainty of the barrier height, the atom numbers and the spacing of the standing light wave lead to a large systematic uncertainty of the coupling constants of  $E_j/h = 2.33$ – $4.14$  kHz,  $E_c/h = 0.30$ – $0.35$  Hz and  $\delta E/h = 0.12$ – $0.16$  mHz.

To initiate the dynamics two different initial population imbalances are prepared by changing the initial position of the harmonic trapping potential with respect to the periodic potential. The shift for accessing the plasma oscillation regime is  $\Delta x = 240(80)$  nm leading to  $n(0) = 161(35)$  and the self-trapping regime  $\Delta x = 500(80)$  nm leading to  $n(0) = 357(35)$ . The critical initial population imbalance is  $n_c = 193$ .

After the preparation of a Bose–Einstein condensate in the asymmetric double-well potential the Josephson dynamics is initiated by moving the harmonic trap to  $\Delta x = 0$  and realizing a symmetric double-well. A motion of the harmonic trap faster than the inverse local trapping frequency might lead due to experimental uncertainties to an uncontrolled excitation of the two Bose–Einstein condensates and thus to an unpredictable time-dependent change of the coupling constants. Hence, in order not to excite any dynamics within the wells the shift is performed slower than the inverse local trapping frequencies of  $2\pi/\omega_{loc} \approx 3$  ms, but much faster than the tunnelling time of about 30 ms. The time constant for moving the harmonic trap is chosen to be  $\tau_{xdt} = 5$  ms with the time dependence of the position

$$x_{xdt}(t) = \Delta x(t) = \Delta x(0) \cdot \exp(-t/\tau_{xdt}). \quad (50)$$

The measurement of the temporal evolution in both dynamical regimes (plasma oscillations and self-trapping) is shown in figure 12. In the Josephson regime (figure 12(a)) both variables show oscillations around a zero mean value. The population imbalance starts with the prepared initial value and the relative phase with zero. In the self-trapping regime as

<sup>1</sup> The difference between the previously [53] reported value of 412(20) Hz and the new value of 420(5) Hz for the barrier height results from an improved method for deducing the height of the standing light wave by using 3D numerical simulations instead of the non-polynomial Schrödinger equation for calibrating  $V_0$ . For details on the calibration method we refer to [54].

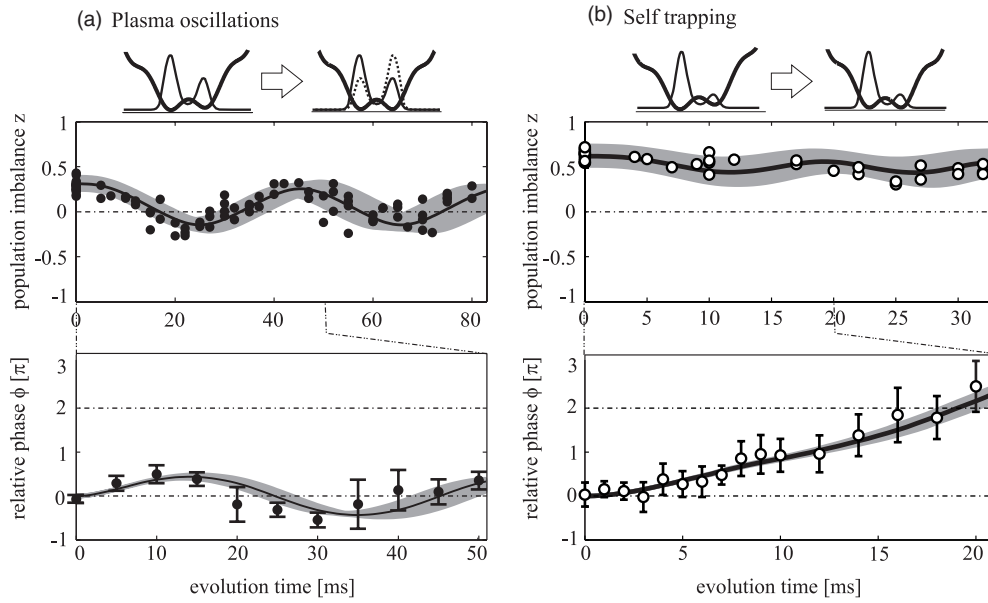


**Figure 12.** Dynamical response of the bosonic Josephson junction. (a) shows the measurement of the temporal evolution of the population imbalance (upper graph) and the relative phase (lower graph) in the Josephson regime. The dynamics is initiated by a population imbalance of  $n(0) = 161(35)$ . Both dynamical variables show oscillations with a zero mean value. The deduced timescale of the oscillations is  $40(2)$  ms. (b) shows the measurement of the temporal evolution of the two dynamical variables in the self-trapping regime, where the dynamics is initiated by a population imbalance of  $n(0) = 357(35)$ . Here the initial population imbalance does not change within the experimental error and the phase winds up. The solid lines correspond to the solution of the full 3D Gross–Pitaevskii equation with only independently measured parameters and also taking the time-dependent position of the harmonic trap into account. However, for quantitative agreement a 40 nm smaller jump of the harmonic trap is assumed, which is well within the experimental error of about 80 nm. The grey shaded area corresponds to the variation of the initial shift of the harmonic trap ( $\pm 40$  nm) and the variation of the total number of atoms (1000 to 1300) within the measured range.

shown in figure 12(b) the population imbalance is locked (within the experimental error) and the phase winds up. The error bars of the relative phases correspond to the standard deviation of the phase measurements.

The theoretical prediction for the temporal evolution is indicated by the solid lines, which are calculated by performing 3D simulations of the Gross–Pitaevskii equation using only the independently measured trap parameters, atom numbers and shifts of the harmonic trap. For quantitative agreement with the experimental data also the shifting time of  $\tau_{sw} = 5$  ms is taken into account. Furthermore, a detailed analysis shows that the harmonic trap does not reach the designated position but stops on average about 40 nm earlier, which is well within the experimental uncertainty of 80 nm. The grey shaded regions in figure 12 correspond to the experimental uncertainties and are calculated by performing numerical simulations of the experiment with different atom numbers at different initial positions of the harmonic trap. The atom numbers range between 1000 and 1300 and the position of the harmonic trap in the plasma oscillation regime is  $-240 \pm 40$  nm (the jump is 200 nm) and in the self-trapping regime of  $-500 \pm 40$  nm (with a jump of 460 nm).

The expected tunnelling frequency according to the two-mode model varies between  $\tau_p = 29$  ms and 37 ms, which is faster than the experimentally found  $40(2)$  ms. This deviation

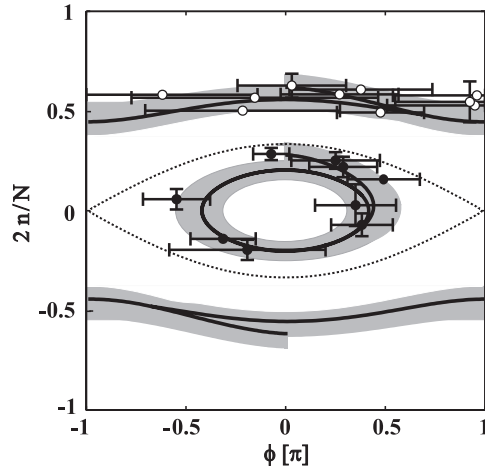


**Figure 13.** Phase plane diagram of the bosonic Josephson junction. In this graph the population imbalance is plotted versus the relative phase. The filled circles correspond to measurements in the Josephson tunnelling regime and the open circles to the measurements in the self-trapping regime. The two regimes are separated by the separatrix (dashed line). The solid lines show the expected behaviour of the dynamical variables due to the two-mode model, where also the time dependence of the shift of the harmonic trapping potential is taken into account. The grey shade area corresponds to the uncertainty of the initial parameters.

might be a result of the change of the transverse size of the matter wave packets during the tunnelling (by  $\sigma_{\min}/\sigma_{\max} = 0.7$ ), which is not taken into account by the two-mode model. However, the amplitudes of the oscillations are correctly accounted for as shown in the phase plane diagram in figure 13, where the normalized population imbalance is plotted versus the relative phase. The filled circles show the data in the plasma oscillation regime and the open circles in the self-trapping regime. The solid lines result from numerical simulations of the two-mode model, where the time-dependent shift of the harmonic trap is taken into account. For this the equation of motion in the case of an energy asymmetry (from equation (35)) are used

$$\frac{d\phi}{dt} = \frac{E_c}{\hbar} n + \frac{E_j}{\hbar} \frac{4n}{N^2} \left( \sqrt{1 - \frac{4n^2}{N^2}} \right)^{-1} \cos(\phi) - \delta \Delta x \quad (51)$$

(the equation of motion of the population imbalance is unchanged and is governed by equation (46)). The time dependence of the position of the harmonic trap is given above (equation (50)). The grey shaded area corresponds to the experimental uncertainty calculated by using the same numerical integration for different initial population imbalances in the Josephson regime  $n(0) = 161 \pm 35$  and in the self-trapping regime  $n(0) = 357 \pm 35$ .

To estimate the effect of the finite shifting time we can solve the equation of motion in the small amplitude limit and find for  $t \gg \tau_{xdt}$  that the temporal evolution of the population imbalance is governed by

$$n(t) = \frac{n(0)}{\sqrt{1 + \tau_{xdt}^2 \omega_p^2}} \times \cos(\omega_p t - \arctan(\omega_p \tau_{xdt})). \quad (52)$$

Thus, the oscillation amplitudes for our parameters are reduced by 25% leading to an effective critical population imbalance of  $n_c = 238$  instead of 193. This can be understood by considering that already during the change of the position of the harmonic trap the tunnelling

dynamics is initiated and thus energy is taken out of the motion. Figure 13 reveals that the dynamical response of the BJJ in the phase plane portrait is very well described by the two-mode model.

## 6. Summary

We discussed the experimental realizations and investigations of a single Josephson junction with Bose–Einstein condensates. The measured static, thermal and dynamical properties are quantitatively compared with the Bose–Hubbard many-particle description and the mean-field model.

We found that the measured steady state population imbalances as a function of the asymmetry of the double-well potential were in quantitative agreement with the theoretical expectation. In further experiments the investigation was focused on the measurement of thermally induced fluctuations of the relative phase in a symmetric double-well. In the high temperature limit, when the thermal energy scale is much larger than the plasma energy associated with small amplitude Josephson oscillations, a semi-classical approach is in excellent agreement with the experimentally measured distributions. Due to the quantitative agreement the measurement of the fluctuations could be applied to measure the temperature of a degenerate Bose gas leading to a new method for thermometry. This new method can also be applied to Bose gases at very low temperatures far below the critical temperature for Bose–Einstein condensation, where standard thermometry methods fail.

By controlling the initial population imbalance the dynamics in the plasma oscillation regime and also the dynamics in the self-trapping regime could be accessed and found to be consistent with the numerical solution of the 3D Gross–Pitaevskii equation. The measured amplitudes of the population imbalance and the relative phase were also in excellent agreement with the prediction of the Gross–Pitaevskii two-mode equations of motion, however the timescale of the tunnelling dynamics deviated. The discrepancy might be explained by the fact that the transverse size of the wave packets changed during the evolution and resulted in a slower tunnelling than expected.

## Acknowledgments

In the presented work many people were involved at different stages of the experiment and the theoretical modelling. We thank the experimentalists M Albiez, J Fölling, B Hemmerling, S Hunsmann, T Ottenstein and for the theoretical support by D Ananikian, T Bergeman, J Esteve, M Scherer and A Trombettoni. This work was funded by the University of Heidelberg, Deutsche Forschungsgemeinschaft Schwerpunktsprogramm SPP1116 and by Landesstiftung Baden-Württemberg Atomoptik. R G thanks the Landesgraduiertenförderung Baden-Württemberg for the financial support.

## Appendix A. Experimental realization of the bosonic Josephson junction

The most direct way to generate a Josephson junction with Bose–Einstein condensates is the realization of a double-well potential for a degenerate Bose gas. If the barrier is high enough, i.e. comparable to the chemical potential of the atoms, the BEC is split into two localized matter wave packets, and if the barrier is not too high, particles can tunnel from well to well leading to a coherent coupling. The main difficulty for the experimental realization is, that the

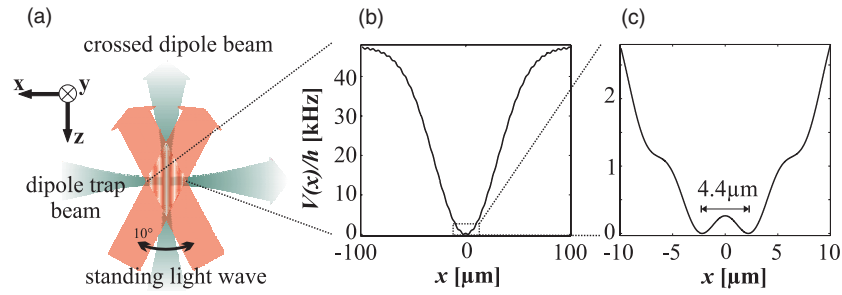


**Figure A1.** Experimental setup and realization of the double-well potential by the superposition of a harmonic trap and an optical lattice with large periodicity. (a) is a sketch of the laser beams generating the optical potentials. Two orthogonal dipole trap beams at 1064 nm (grey) create a 3D harmonic confinement and two laser beams at 830 nm crossing under an angle of about  $10^\circ$  generate the optical lattice (red) with a periodicity of  $d_{sw} \approx 5 \mu\text{m}$ . (b) shows the potential resulting from the superposition of the dipole trap and the optical lattice on the scale of the Gaussian dipole trap beam. (c) is the potential in the centre revealing the symmetric double-well structure with a separation of the two wells of about  $4.4 \mu\text{m}$ .

shape of this potential has to be fixed very well, as the tunnelling current depends exponentially on the barrier height.

A promising method for creating double-well potentials for neutral atoms was presented in the group of J Schmiedmayer in 2005. Their approach is the application of radio-frequency dressed state potentials on an atom chip [55], which in analogy to optical dipole traps, where two electronic states are coupled to each other, address two hyperfine levels. Recently these potentials were employed for coherent splitting of a Bose–Einstein condensate and for matter wave interference experiments [56].

Another possibility of realizing a weak link between two spatially separated Bose–Einstein condensates was demonstrated in 2005 in the group of W Ketterle [57]. They generated a double-well potential where no direct spatial tunnelling between the two Bose–Einstein condensates was possible. Via two Bragg beams atoms were coupled out from both wells coherently and brought to interfere with the two Bose–Einstein condensates, leading to a coherent coupling and establishing the weak link.

The approach used in our experiments is the realization of an all-optical double-well potential, generated by the superposition of a 3D harmonic trapping potential and a periodic potential with large periodicity as depicted in figure A1(a). The effective potential is shown in figure A1(b) on the full scale of the trap and in (c) on the scale of the BEC.

The 3D harmonic trap is generated by two crossed Gaussian Nd:YAG-laser beams at  $\lambda_{\text{Nd:YAG}} = 1064 \text{ nm}$ . The first dipole trap beam, in the following called the wave guide (WG) is responsible for the transverse confinement and points perpendicular to gravity in order to hold the atoms in the trap. The atoms are located at the waist of the beam which has a size of about  $60 \mu\text{m}$  and a power of less than 500 mW. The resulting trapping frequencies can be adjusted to be between typically  $2\pi \times 70 \text{ Hz}$  and  $2\pi \times 180 \text{ Hz}$ . The second dipole trap beam, in the following referred to as the crossed dipole trap (XDT), is pointed perpendicular to the first beam and perpendicular to gravity. The XDT is elliptic, with the tighter confinement in the direction along the WG in order not to influence the transverse trapping. The size of the beam along the WG is  $70 \mu\text{m}$  and in the direction of gravity  $140 \mu\text{m}$  and has a power of typically less than 800 mW. Both beams are transferred to the experiment via optical fibres and the out-coupler of the XDT is fixed on a piezo actuated mount, which allows for changing the

position of the longitudinal confinement over several  $\mu\text{m}$ . The periodic potential is realized by the interference of two titanium-sapphire laser beams at  $\lambda_{\text{Ti:Sa}} = 830 \text{ nm}$ , crossed under an angle of about  $10^\circ$ . The periodicity of the resulting sinusoidal potential is about  $5 \mu\text{m}$ . The waist of the two beams is  $500 \mu\text{m}$  and their power is less than  $100 \text{ mW}$ , leading to a maximal potential height of  $V_{0/h} = 10 \text{ kHz}$ .

The Bose–Einstein condensate consists of typically 1000 to 3000 87-Rubidium atoms, which are pre-cooled in a TOP (time orbiting potential) trap and then adiabatically transferred into the crossed dipole trap, where Bose–Einstein condensation is reached by forced evaporation. The lowest temperatures in the final stage of evaporative cooling are on the order of  $10 \text{ nK}$ .

The imaging of the BEC is done by illuminating the atoms with resonant light at high intensities  $I_0 \gg I_{\text{sat}}$  for  $5 \mu\text{s}$  and deducing the density distribution from the loss of photons from the coherent beam. The imaging is done using a lens system with which the distribution is magnified by 1:10 and projected onto a CCD-camera with a pixel size of  $6.45 \mu\text{m} \times 6.45 \mu\text{m}$ . The optical resolution is about  $3 \mu\text{m}$  and limited by the numerical aperture of the lens.

High stability of the experimental setup is crucial for the realization of the bosonic Josephson junction, especially the parameters of the double-well potential have to be fixed very well, as the tunnelling times and coupling constants depend strongly on the exact shape of the potential. Thus, for the realization of the BJJ the high passive stability of the experimental apparatus is supported by active stabilization of the relevant components. The intensity of the laser fields creating the double-well potential, namely the two dipole trap beams and the two standing light wave beams, is actively stabilized by adjusting the beam intensities with AOMs. The intensity of every beam is monitored with photo-diodes and stabilized by feeding back the signal using a PI-loop. The stability reached is better  $10^{-4}$ . The exact positions of the maxima of the standing light wave are directly connected to the symmetry of the double-well potential and already changes of the optical path of the beams on the  $50 \text{ nm}$  scale lead to modifications of the symmetry of the resulting potential. Thus, the phase of the standing light wave is actively stabilized as well.

The symmetry of the resulting double-well potential is adjusted by changing the position of the harmonic confinement and measuring directly the symmetry of the steady state density distribution of the Bose–Einstein condensate in the double-well. To guarantee that the double-well potential has the right symmetry, check measurements are performed after every 10–20 experiments. For a more detailed discussion on the experimental procedure we refer to [58].

## Appendix B. Measurement of the population imbalance and the relative phase

In our experiments all relevant quantities are deduced from images of either the density distribution in the trap or the density distribution after a time of flight, which in the far field corresponds to the momentum distribution. The population imbalance is obtained by fitting two overlapping Gaussian functions to the density distribution. However, the accuracy of the fitting is not very good, as the separation of the two matter wave packets in the double-well trap (about  $4.4 \mu\text{m}$ ) is only slightly larger than the optical resolution (about  $3 \mu\text{m}$ ) and the barrier height is comparable to the chemical potential leading to broad matter wave packets. To improve the accuracy the distance between the two wave packets is increased by rapidly ramping up the height of the standing light wave (within  $200 \mu\text{s}$ ) and simultaneously turning off the longitudinal confinement (XDT). The minima of the two wells move apart and a dipolar oscillation of the two matter wave packets is induced. As the two BEC move in opposing directions their distance increases and the overlap of the two matter wave packets is reduced. The images are taken when their separation is maximal.

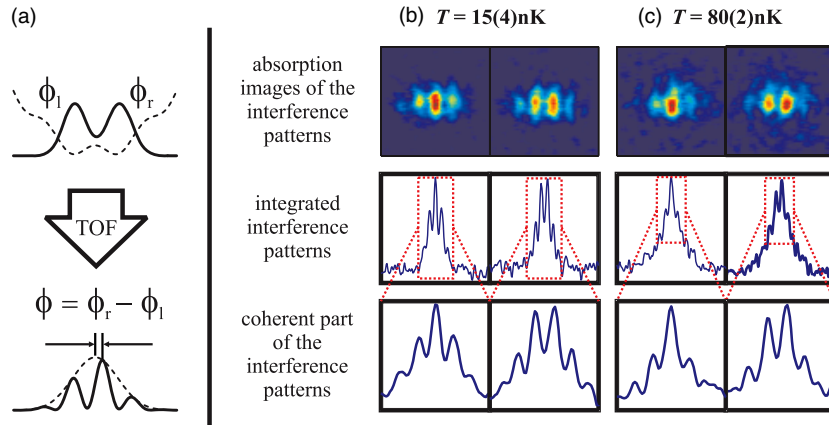


**Figure B1.** Matter wave interference patterns. (a) A sketch of the interference experiments. Once the double-well trap is turned off, the matter wave packets expand, overlap and interfere revealing the relative phase as a shift of the interference peaks with respect to their envelope; (b) corresponds to typical interference patterns at  $\phi \approx 0$  and  $\phi \approx \pi$  for low temperature and (c) to typical interference patterns for high temperature. The integrated patterns show a clear interference signal for all temperatures (central graphs). However, for high temperature also a broad background is visible, corresponding to the distribution of the thermal atoms after the expansion time. In order to find the coherent interference patterns, this background is subtracted (lower graphs).

The relative phase is deduced from time-of-flight images as shown in figure B1(a). The atoms are released from the double-well trap by turning off all potentials within  $200\ \mu\text{s}$  and taking the images after a time-of-flight of between 5 and 8 ms. During this time the matter wave packets fall down, but also expand due to the stored kinetic and interaction energy and interfere with each other. Typical interference patterns are shown in figure B1(b) and for high temperature in (c). The upper part of the graph shows the absorption images, where in (b) the interference patterns are very clear but in (c) a broad background is visible. The middle part of the graphs corresponds to the transversally integrated interference profiles revealing that for high temperature the interference patterns are on top of the thermal background, making an accurate phase deduction difficult. Thus, the thermal background is fitted transversally and subtracted from the interference patterns. The resulting profiles are shown in the lower part of the graphs revealing that the visibility of the interference patterns is mainly independent on temperature and is typically between 40% and 50%.

### Appendix C. Thermalization and thermometry

The measurement of the thermally induced fluctuations can be used for thermometry, even for very low temperatures, where the standard time-of-flight method is not applicable due to the small number of thermal particles. However, even for these temperatures the barrier height can be tuned such that the BJJ becomes sensitive to thermally induced processes and the distribution of the relative phases can be measured. The temperature is then found by calculating the tunnelling coupling numerically and comparing the coherence factor with the theoretical prediction. However, one difficulty for such experiments is the adiabatic preparation of the BJJ. For very low temperatures the tunnelling coupling has to be very small ( $E_j < 3k_B T$ ) in order to allow for the observation of phase fluctuations and the tunnelling

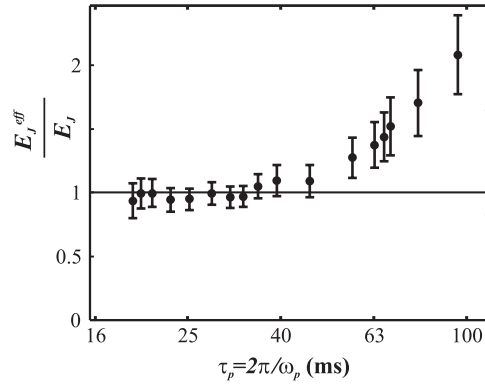


**Figure C1.** Experimental test for thermal equilibration of the BJJ. The graph shows the measured coherence factors as a function of the tunnelling time. The experimental  $E_j^{\text{eff}}$  are deduced by fitting the measured coherence factor with the theoretical prediction. For tunnelling times  $\tau_p \ll 50$  ms the ratio is one. For  $\tau_p > 50$  ms the ratio increases as the BJJ is not completely thermalized. Thermalization takes place only if  $\tau_p \ll t_{\text{ramp}} = 300$  ms, which is the time for ramping up the potential barrier.

time becomes very long. Thus, in order to keep the BJJ in the thermal equilibrium during the preparation, the barrier has to be raised much slower than the typical tunnelling time.

To test on what timescale the ramping has to be performed in order to keep the BJJ in the thermal equilibrium, we compare the coherence factor measurements with the theoretical prediction from equation (41). We introduce an effective tunnelling coupling  $E_j^{\text{eff}}$  to account for out of equilibrium situations and deduce  $k_B T / E_j^{\text{eff}}$  from the experimental data shown in figure 8. In figure C1 the ratio  $E_j^{\text{eff}} / E_j$  is plotted as a function of the tunnelling time  $\tau_p = 2\pi / \omega_p \propto 1 / \sqrt{E_j}$ . We find that for the chosen ramping time of 300 ms the effective tunnelling coupling is only equal to the expected tunnelling coupling for  $\tau_p < 50$  ms. The observed increase of  $E_j^{\text{eff}}$  for large tunnelling times ( $\tau_p > 50$  ms which corresponds to  $E_j < 60$  nK) could be explained by the fact that the system might still not have reached the equilibrium after the 300 ms ramp.

The applicability of the thermometer is demonstrated by observing the heating up of a degenerate Bose gas in a 3D harmonic trapping potential and comparing the temperatures deduced from the phase fluctuations measurements with independent time-of-flight temperature measurements. Agreement within the experimental error is found in the region, where both methods can be applied. For more details on the realization of this primary phase noise thermometer we refer to [54].

## References

- [1] Josephson B D 1962 Possible new effects in superconducting tunneling *Phys. Lett.* **1** 251
- [2] Anderson P W and Rowell J M 1963 Probable observation of the Josephson superconducting tunneling effect *Phys. Rev. Lett.* **10** 230
- [3] Likharev K K 1979 Superconducting weak links *Rev. Mod. Phys.* **51** 101
- [4] Barone A and Paterno G 1982 *Physics and Applications of the Josephson Effect* (New York: Wiley)
- [5] Pereverzev S, Loshak A, Backhaus S, Davis J C and Packard R E 1997 Quantum oscillations between two weakly coupled reservoirs of superfluid  $^3\text{He}$  *Nature* **388** 449
- [6] Backhaus S, Pereverzev S, Loshak A, Davis J C and Packard R E 1997 Direct measurement of the current-phase relation of a superfluid  $^3\text{He}$ -B weak link *Science* **278** 1435
- [7] Davis J C and Packard R E 2002 Superfluid  $^3\text{He}$  Josephson weak links *Rev. Mod. Phys.* **74** 741

- [8] Sukhatme K, Mukharsky Y, Chui T and Pearson D 2001 Observation of the ideal Josephson effect in superfluid  $^4\text{He}$  *Nature* **411** 280
- [9] Anderson M, Ensher J, Matthews M, Wieman C and Cornell E 1995 Observation of Bose-Einstein condensation in a dilute atomic vapor *Science* **269** 198
- [10] Davis K, Mewes M-O, Andrews M, van Druten N, Durfee N, Kurn D and Ketterle W 1995 Bose-Einstein condensation in a gas of sodium atoms *Phys. Rev. Lett.* **75** 3969
- [11] Bradley C C, Sackett C A, Tollet J J and Hulet R G 1995 Evidence of Bose-Einstein condensation in an atomic gas with attractive interactions *Phys. Rev. Lett.* **75** 1687
- [12] Javanainen J 1986 Oscillatory exchange of atoms between traps containing Bose condensates *Phys. Rev. Lett.* **57** 3164
- [13] Streltsov A I, Alon O E and Cederbaum L S 2006 General variational many-body theory with complete self-consistency for trapped bosonic systems *Phys. Rev. A* **73** 063626
- [14] Masiello D, McKagan S B and Reinhardt W P 2005 Multiconfigurational Hartree-Fock theory for identical Bosons in a double well *Phys. Rev. A* **72** 063624
- [15] Ananikian D and Bergeman T 2006 Gross-Pitaevskii equation for Bose particles in a double-well potential: two-mode models and beyond *Phys. Rev. A* **73** 013604
- [16] Spekkens R W and Sipe J E 1999 Spatial fragmentation of a Bose-Einstein condensate in a double-well potential *Phys. Rev. A* **59** 3868
- [17] Jack M W, Collett M J and Walls D F 1996 Coherent quantum tunneling between two Bose-Einstein condensates *Phys. Rev. A* **54** R4625
- [18] Milburn G J, Corney J, Wright E M and Walls D F 1997 Quantum dynamics of an atomic Bose-Einstein condensate in a double-well potential *Phys. Rev. A* **55** 4318
- [19] Ruostekoski J and Walls D F 1998 Bose-Einstein condensate in a double-well potential as an open quantum system *Phys. Rev. A* **58** R50
- [20] Paraoanu Gh-S, Kohler S, Sols F and Leggett A J 2001 The Josephson plasmon as a Bogoliubov quasiparticle *At. Mol. Opt. Phys.* **34** 4689
- [21] Leggett A J 2001 Bose-Einstein condensation in the alkali gases: some fundamental concepts *Rev. Mod. Phys.* **73** 307
- [22] Mahmud K W, Perry H and Reinhardt W P 2005 Quantum phase-space picture of Bose-Einstein condensates in a double well *Phys. Rev. A* **71** 023615
- [23] Cirac J I, Lewenstein M, Mølmer K and Zoller P 1998 Quantum superposition states of Bose-Einstein condensates *Phys. Rev. A* **57** 1208
- [24] Steel M J and Collett M J 1998 Quantum state of two trapped Bose-Einstein condensates with a Josephson coupling *Phys. Rev. A* **57** 2920
- [25] Dunningham J A, Burnett K and Edwards M 2001 Relative number squeezing in Bose-Einstein condensates *Phys. Rev. A* **64** 015601
- [26] Mahmud K W, Perry H and Reinhardt W P 2003 Phase engineering of controlled entangled number states in a single component Bose-Einstein condensate in a double well *J. Phys. B: At. Mol. Opt. Phys.* **36** 265
- [27] Streltsov A I, Cederbaum L S and Moiseyev N 2004 Ground-state fragmentation of repulsive Bose-Einstein condensates in double-trap potentials *Phys. Rev. A* **70** 053607
- [28] Zhang W-M, Feng D H and Gilmore R 1990 Coherent states: theory and some applications *Rev. Mod. Phys.* **62** 867
- [29] Amico L and Penna V 1998 Dynamical mean field theory of the Bose-Hubbard model *Phys. Rev. Lett.* **80** 2189
- [30] Buonsante P, Penna V and Vezzani A 2005 Attractive ultracold Bosons in a necklace optical lattice *Phys. Rev. A* **72** 043620
- [31] Penrose O and Onsager L 1956 Bose-Einstein condensation and liquid helium *Phys. Rev.* **104** 576
- [32] Nozières P 1982 *Bose-Einstein Condensation* ed A Griffin, D W Snoke and S Stringari (Cambridge: Cambridge University Press)
- [33] Mueller E J, Ho T-L, Ueda M and Baym G 2006 Fragmentation of Bose-Einstein condensates *Phys. Rev. A* **74** 033612
- [34] Castin Y and Dalibard J 1997 Relative phase of two Bose-Einstein condensates *Phys. Rev. A* **55** 4330
- [35] Barnett S M and Pegg D T 1986 Phase in quantum optics *J. Phys. A: Math. Gen.* **19** 3849
- [36] Pegg D T and Barnett S M 1989 Phase properties of the quantized single-mode electromagnetic field *Phys. Rev. A* **39** 1665
- [37] Pitaevskii L and Stringari S 2001 Thermal versus quantum decoherence in double well trapped Bose-Einstein condensates *Phys. Rev. Lett.* **87** 180402
- [38] Gati R, Hemmerling B, Fölling J, Albiez M and Oberthaler M K 2006 Noise thermometry with two weakly coupled Bose-Einstein condensates *Phys. Rev. Lett.* **96** 130404

- [39] Ambegaokar V and Baratoff A 1963 Tunneling between superconductors *Phys. Rev. Lett.* **10** 486
- [40] Wright E M, Walls D F and Garrison J C 1996 Collapses and revivals of Bose-Einstein condensates formed in small atomic samples *Phys. Rev. Lett.* **77** 2158
- [41] Imamoğlu A, Lewenstein M and You L 1997 Inhibition of coherence in trapped Bose-Einstein condensates *Phys. Rev. Lett.* **78** 2511
- [42] Javanainen J and Wilkens M 1997 Phase and phase diffusion of a split Bose-Einstein condensate *Phys. Rev. Lett.* **78** 4675
- [43] Javanainen J and Ivanov M Yu 1999 Splitting a trap containing a Bose-Einstein condensate: atom number fluctuations *Phys. Rev. A* **60** 2351
- [44] Smerzi A, Fantoni S, Giovanazzi S and Shenoy S R 1997 Quantum coherent atomic tunneling between two trapped Bose-Einstein condensates *Phys. Rev. Lett.* **79** 4950
- [45] Zapata I, Sols F and Leggett A J 1998 Josephson effect between trapped Bose-Einstein condensates *Phys. Rev. A* **57** R28
- [46] Raghavan S, Smerzi A, Fantoni S and Shenoy S R 1999 Coherent oscillations between two weakly coupled Bose-Einstein condensates: Josephson effects,  $\pi$  oscillations, and macroscopic quantum self-trapping *Phys. Rev. A* **59** 620
- [47] Ostrovskaya E A, Kivshar Y S, Lisak M, Hall B, Cattani F and Anderson D 2000 Coupled-mode theory for Bose-Einstein condensates *Phys. Rev. A* **61** 031601
- [48] Giovanazzi S, Smerzi A and Fantoni S 2000 Josephson effects in dilute Bose-Einstein condensates *Phys. Rev. Lett.* **84** 4521
- [49] Anglin J R, Drummond P and Smerzi A 2001 Exact quantum phase model for mesoscopic Josephson junctions *Phys. Rev. A* **64** 063605
- [50] Williams J E 2001 Optimal conditions for observing Josephson oscillations in a double-well Bose-Einstein condensate *Phys. Rev. A* **64** 013610
- [51] Anderson B P and Kasevich M A 1998 Macroscopic quantum interference from atomic tunnel arrays *Science* **282** 1686
- [52] Cataliotti F S, Burger S, Fort C, Maddaloni P, Minardi F, Trombettoni A, Smerzi A and Inguscio M 2001 Josephson junction arrays with Bose-Einstein condensates *Science* **293** 843
- [53] Albiez M, Gati R, Fölling J, Hunsmann S, Cristiani M and Oberthaler M K 2005 Direct observation of tunneling and nonlinear self-trapping in a single bosonic Josephson junction *Phys. Rev. Lett.* **95** 010402
- [54] Gati R, Esteve J, Hemmerling B, Ottenstein T B, Appmeier J, Weller A and Oberthaler M K 2006 A primary noise thermometer for ultracold Bose gases *New. J. Phys.* **8** 189
- [55] Hofferberth S, Lesanovsky I, Fischer B, Verdu J and Schmiedmayer J 2006 Radiofrequency-dressed-state potentials for neutral atoms *Nat. Phys.* **2** 710
- [56] Schumm T, Hofferberth S, Andersson L M, Wildermuth S, Groth S, Bar-Joseph I, Schmiedmayer J and Krüger P 2005 Matter-wave interferometry in a double well on an atom chip *Nat. Phys.* **1** 57
- [57] Shin Y, Jo G-B, Saba M, Pasquini T A, Ketterle W and Pritchard D E 2005 Optical weak link between two spatially separated Bose-Einstein condensates *Phys. Rev. Lett.* **95** 170402
- [58] Gati R, Albiez M, Fölling J, Hemmerling B and Oberthaler M K 2006 Realization of a single Josephson junction for Bose-Einstein condensates *Appl. Phys. B* **82** 207